

# Flooding and inundation maps using interpolated CYGNSS reflectivity observations

Clara Chew<sup>a,b,\*</sup>, Eric Small<sup>c</sup>, Hannah Huelsing<sup>a</sup>

<sup>a</sup> University Corporation for Atmospheric Research, 3090 Center Green Dr, Boulder, CO 80301, USA

<sup>b</sup> Muon Space, 2250 Charleston Rd, Mountain View, CA 94043, USA

<sup>c</sup> University of Colorado Boulder, Department of Geological Sciences, 2200 Colorado Ave, Boulder, CO 80309, USA

## ARTICLE INFO

Edited by Menghua Wang

### Keywords:

Flooding  
Inundation  
GNSS reflectometry  
CYGNSS  
Microwave

## ABSTRACT

Despite the myriad of remote sensing techniques currently used to map surface water, a gap remains in our ability to rapidly map inundation from flooding at the required temporal resolution to understand how floods evolve. However, the recent launch of constellations of Global Navigation Satellite System-Reflectometry (GNSS-R) satellites can provide data at a more frequent temporal repeat than a single satellite. These L-band instruments could provide moderate spatial resolution inundation maps at a better temporal resolution than other satellite radars. This paper describes a retrieval algorithm for flood inundation mapping using GNSS-R data from the Cyclone GNSS (CYGNSS) constellation. The algorithm employs a simple dielectric model to retrieve fractional inundation from an observation of reflectivity, requiring parameterizations of soil surface and water roughness as well as ancillary soil moisture data. Here, we give a brief overview of the model, describe our parameterization scheme, and present inundation maps using CYGNSS data. We describe four case studies (from the Amazon, Mozambique, Mali, and Australia) and compare the CYGNSS inundation maps to other surface water data (SWAMPS, PALSAR-2, Dartmouth Flood Observatory, MODIS, and the Global Surface Water Explorer). We identify sources of uncertainty in the CYGNSS inundation maps and discuss possible reasons for discrepancies between the inundation retrievals. We introduce the data portal, which houses the CYGNSS inundation maps, for use by the science community.

## 1. Introduction

### 1.1. Inundation mapping

Mapping the extent and duration of surface flooding and inundation is important for numerous societal and scientific applications, ranging from understanding feedbacks between seasonal changes in wetlands and the emission of methane to pinpointing communities most affected by extreme weather events in near real time (Baqir et al., 2012; Durack et al., 2012; Melton et al., 2013; Ringeval et al., 2010; Shindell et al., 2004). A myriad of approaches for mapping surface water already exists, and the favored approach depends on the environmental conditions and desired spatiotemporal resolution of the information.

In situ observations, which are point measurements, may be made during field campaigns or after a flood has receded. These observations are difficult to collect and generally not collected with any regularity. Because of this, satellite remote sensing is often the tool of choice for

mapping surface water, but these data also come with caveats depending on the specific type of remote sensing to be used. Optical indices, which can be very successful at mapping open water, underestimate the extent of surface water globally as they often fail to sense water beneath vegetation (Lefebvre et al., 2019), and there is significant disagreement in the delineation of surface water in wetlands among the different indices (Nakaegawa, 2012). Optical data are also obscured by cloud cover, which degrades the temporal revisit time in the often cloud-covered tropics and usually prevents the data from being used during extreme weather events. In an attempt to mitigate cloud cover issues, data products from optical sensors are often produced as an aggregation of data over longer time windows, though this is often not sufficient in the tropics or northern high latitudes, where clouds can be present for months at a time.

Data from microwave remote sensing instruments (i.e., radiometers or active radar) can penetrate some amount of vegetation cover and are insensitive to clouds, and there is a long history of researchers using

\* Corresponding author at: Muon Space, 2250 Charleston Rd, Mountain View, CA 94043, USA.

E-mail address: [clara@muonspace.com](mailto:clara@muonspace.com) (C. Chew).

<https://doi.org/10.1016/j.rse.2023.113598>

Received 2 October 2022; Received in revised form 14 April 2023; Accepted 18 April 2023

Available online 17 May 2023

0034-4257/© 2023 Elsevier Inc. All rights reserved.

these techniques to map inundation and flooding (e.g., (Prigent et al., 2001; Schroeder et al., 2015)). However, these data also have their limitations. Inundation products derived from radiometers like GIEMS-2 (Prigent et al., 2020) or SWAMPsv3 (Jensen and McDonald, 2019) are spatially coarse (>25 km). Depending on the time-averaging window, these products are either produced monthly (GIEMS-2) or daily (SWAMPsv3, though the actual temporal repeat is ~3 days). Flood maps derived from active radar like Sentinel-1, a C-band SAR, have the advantage of coming with a very fine spatial resolution (tens of m) but at the expense of a low temporal repeat (>1 week) (e.g., (Muro et al., 2016; Tsyganskaya et al., 2018)). NASA’s upcoming NISAR mission, a combined L- and S-band active radar system, will have the same fine spatial resolution as Sentinel-1 but with a longer wavelength and increased vegetation penetration capability. Though, NISAR data will also come with the low temporal repeat frequency. For many applications, weekly revisits are sufficient—mapping seasonal changes in wetland extent or gradual changes in reservoir levels generally do not require data that are updated more frequently.

Mapping surface flooding from extreme weather events does require shorter revisit times. Depending on the severity of the event, floodwaters may have already risen and receded within the span of several days, which means that flooding maps derived from active radar like Sentinel-1, NISAR, or otherwise, might serendipitously capture a snapshot of the event, but they cannot monitor the evolution of the flood, and it is difficult to know if the observations captured the extent of maximum flooding. Radiometer data are generally considered to be too coarse for mapping inundation from flooding except for very large events (Du et al., 2018). And, optical data, despite also having similar spatial resolution to active radar with a daily temporal repeat, often cannot be used due to the severe flooding events usually being associated with heavy cloud cover.

### 1.2. CYGNSS

Here we will describe an inundation dataset that is not constrained to the tradeoff in spatial and temporal resolution described above. We use a relatively new technique called Global Navigation Satellite System-Reflectometry (GNSS-R) that is currently employed by the Cyclone GNSS (CYGNSS) satellite constellation. Although this technique has its own unique limitations, which we will describe, it could also help fill the current gap in flood mapping from satellites and provide complementary inundation information to that which is already available.

CYGNSS, NASA’s first Earth Venture Class Mission, was launched in

December of 2016 for the purpose of retrieving ocean surface wind speed during hurricanes and tropical storms. Each one of CYGNSS’ eight satellites carries two downward-looking antennas and a GNSS-R receiver, which records surface reflected GNSS signals. GNSS is an umbrella term for the various constellations of navigation satellites (e.g., the United States’ Global Positioning System (GPS) satellites). Signals from the GPS constellation, which CYGNSS was designed to receive, are L-band microwave signals, which are transmitted at right-handed circular polarization (RHCP) but are predominantly left-handed circular polarization (LHCP) upon reflection. The LHCP antennas onboard CYGNSS capture these surface-reflected GPS signals, and then scientists use them to infer information about the reflecting surface (Fig. 1).

Depending on the properties of the surface, the reflected GPS signal will change. Smooth surfaces produce specular reflections, with most of the reflected signal’s energy directed towards the receiving antenna. Conversely, rougher surfaces produce diffuse reflections, which results in a weaker reflection. This sensitivity to surface roughness is one of the reasons why GNSS-R was chosen as the technology of choice for monitoring ocean surface wind speed with CYGNSS—stronger winds generally produce larger waves and rougher surfaces, and by correlating the amplitude of the reflected signal with ocean surface roughness, one can retrieve wind speed (Clarizia and Ruf, 2016; Ruf et al., 2013).

Another compelling reason for utilizing GNSS-R for this task is that it’s an economical choice compared to other satellite remote sensing techniques. Because the transmitters are already on orbit, receivers can be manufactured and launched for the fraction of the price of a traditional L-band satellite. This makes constellations of satellites feasible, and constellations of satellites lower the temporal repeat time, an important factor in monitoring rapidly-developing extreme weather events.

In addition to roughness, another important property of the surface affects reflected GPS signals: the dielectric constant. At L-band, the dielectric constant of most natural surfaces is primarily a function of the amount of water either in or on the land surface, which is why several satellites specifically designed for monitoring surface hydrology use L-band sensors (e.g., SMAP, SMOS, NISAR). Surfaces with higher dielectric constants, either from having higher soil moisture or more water on the surface, produce stronger reflections and vice versa (Ulaby et al., 1986). L-band signals are also able to penetrate denser vegetation than shorter wavelengths like C- or X-band, which are employed by other sensors like Sentinel-1. Leading up to the launch of CYGNSS, a handful of studies had explored the potential of spaceborne GNSS-R to retrieve either soil moisture or map surface water (Camps et al., 2016; Chew et al., 2016;

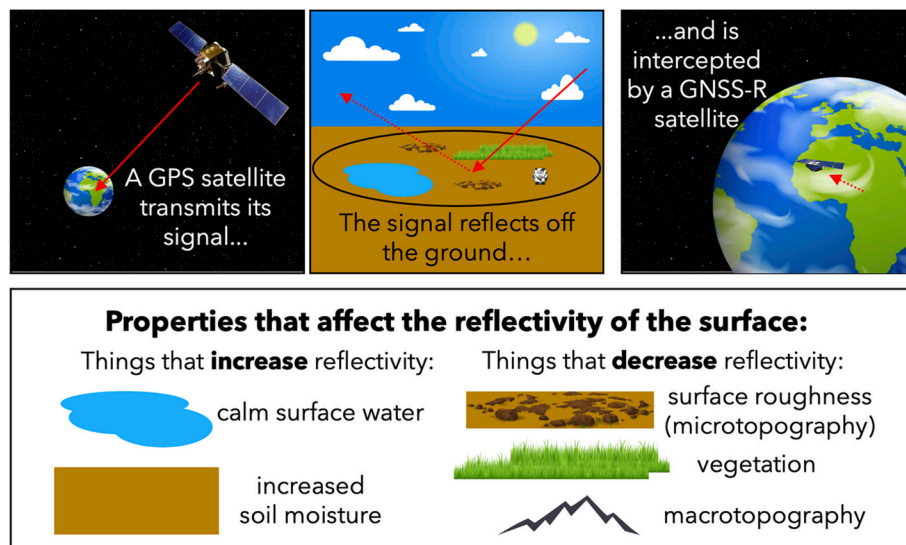
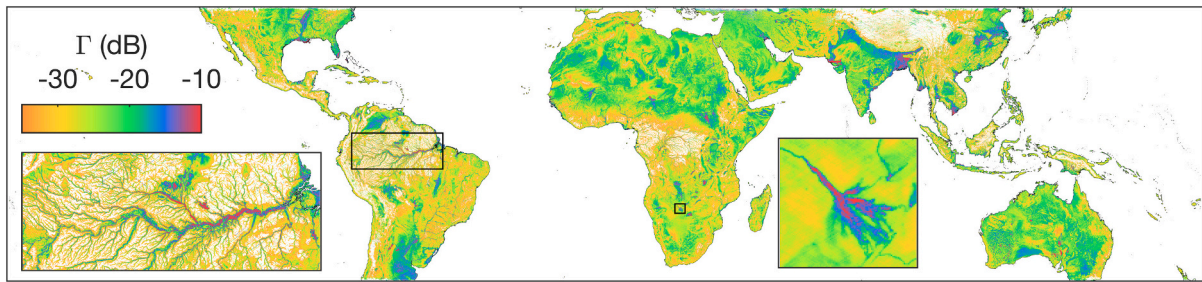


Fig. 1. Information about the GNSS-R scattering geometry (top row) and surface characteristics that affect the reflected signal (bottom row).



**Fig. 2.** Mean 3 km gridded map of  $\Gamma$  observations for the year 2020. Black boxes indicate regions shown in the insets (the Amazon and Okavango Delta, from left to right). Higher values of  $\Gamma$  are observed in wet, topographically flat areas, and areas without significant vegetation. Few observations are found in high altitude regions exceeding 3000 m (e.g., Tibetan Plateau) due to software limitations. Data quality controls removed observations with very low signal (SNR < 2 dB), resulting in few observations in densely vegetated forests (e.g., the Amazon, Central Africa, and Indonesia) aside from pixels containing standing water. Areas with data below the quality control thresholds are shown in white.

Gleason et al., 2005), but these studies were in the minority compared to the amount of work done exploring GNSS-R and ocean remote sensing.

However, once CYGNSS was launched, CYGNSS observations of surface reflectivity ( $\Gamma$ ) over land surprisingly exhibited a strong sensitivity to surface water features, some as small as 100–200 m wide (Fig. 2), due to the coherency of the reflected signal over smooth surfaces (Chew and Small, 2018). This led to several studies investigating the ability of CYGNSS to map inland surface water (e.g., (Al-Khaldi et al., 2021; Chapman et al., 2022; Chew et al., 2018; Gerlein-Safdi and Ruf, 2019; Li et al., 2022; Li et al., 2021; Morris et al., 2019; Rodriguez-Alvarez et al., 2019; Wan et al., 2019; Zeiger et al., 2022; Zhang et al., 2021)). In addition, sensitivity to near-surface soil moisture was also identified (e.g., (Al-Khaldi et al., 2019; Chew and Small, 2018; Clarizia et al., 2019; Eroglu et al., 2019; Kim and Lakshmi, 2018; Senyurek et al., 2020; Yan et al., 2020)). This solidified the interest in using spaceborne GNSS-R observations to retrieve geophysical variables related to terrestrial hydrology. There are now several GNSS-R missions that are either being developed by other governmental agencies (e.g., ESA’s HydroGNSS mission (Unwin et al., 2021)) or private companies (e.g., Spire, Muon Space) that also aim to retrieve similar hydrologic information.

Here, we present an algorithm to map surface flooding and inundation using CYGNSS data. The algorithm takes a CYGNSS observation and ancillary information about soil moisture and surface roughness and uses these as input to a simple model that retrieves fractional surface inundation for a  $3 \times 3$  km grid cell anywhere within the inclination of CYGNSS ( $\pm 38$  degrees latitude). We will describe our process for parameterization of the model, calibration and comparison inundation data, the errors and uncertainties in our inundation retrievals, and how to access them. Finally, we discuss plans to improve the GNSS-R inundation retrievals, not only from CYGNSS but from future satellites like it.

## 2. Methods

### 2.1. CYGNSS data

Because inundation mapping using spaceborne GNSS-R data is still a relatively nascent field, there is no one ‘industry standard’ approach to derive inundation maps. Instead, a variety of approaches have been suggested or tried. These approaches tend to use one of a few different variables derived from delay-Doppler maps (DDMs) produced by spaceborne GNSS-R receivers like CYGNSS. Our algorithm uses surface reflectivity ( $\Gamma$ ), which is the peak value of the DDM ( $P^c$ ), which is then corrected for receiver antenna gain ( $G^r$ ), the GPS L1 wavelength ( $\lambda$ ), GPS effective isotropic radiated power ( $P^e G^e$ ), and bistatic range ( $R_{ts} + R_{sr}$ ) assuming coherent reflections (De Roo and Ulaby, 1994):

$$\Gamma = \frac{4\pi(R_{ts} + R_{sr})^2}{P^e G^e} \frac{4\pi P^c}{G^r \lambda^2} \quad (1)$$

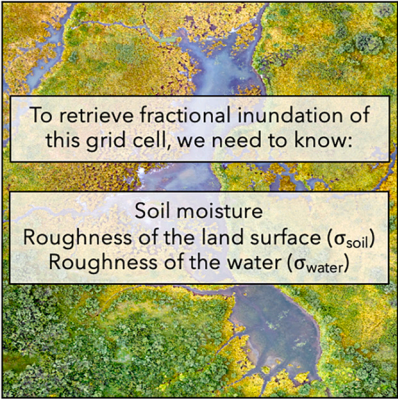
$\Gamma$  is very commonly reported in decibels (dB).

Although not shown in Eq. (1), the incidence angle ( $\theta$ ) of the reflected signal affects the relationship between  $\Gamma$  and the surface dielectric constant (more details below and in Box 1). Here, we correct for the effect of  $\theta$  on  $\Gamma$ , as has been done in previous studies (e.g., (Al-Khaldi et al., 2019; Chew and Small, 2020a)). Assuming coherent reflections and a smooth reflecting surface, the relationship between  $\theta$  and  $\Gamma$  can be modeled (Fig. S1). The effects of soil moisture on this relationship are negligible. Using this relationship, we correct our  $\Gamma$  observations for  $\theta$  normalized to 25 degrees. For observations between  $\sim 0$ – $40$  degrees, this correction is small— $< 0.1$  dB. As  $\theta$  increases, so does the magnitude of the correction.

CYGNSS spatial footprints are, for coherent reflections, a minimum of  $3.5 \times 0.5$  km large (see Supplement for a discussion on the footprint). Although the eight CYGNSS satellites sample both the ocean and land surface at all hours of the day, there are not enough of them (or enough receive channels on each instrument) to completely sample the surface within the span of a few days given this spatial footprint. Examples of typical spatial distributions of observations gridded at  $3 \times 3$  km over three days are shown in Fig. 3a,b. Our goal is to provide a framework for which rapidly-updated inundation maps can be examined for areas potentially impacted by flooding. We selected a data aggregation period of 3 days to balance the competing needs of adequate spatial coverage and rapid updates to map the evolution of inundation events.

Even using a data aggregation period of three days results in maps that are sparse enough that they are difficult to visually assess (i.e., Fig. 3a,b). In order to produce spatially-complete inundation maps, we first spatially interpolated CYGNSS observations over 3-day windows using the Previously-Observed Behavior Interpolation (POBI) method (Chew, 2021). POBI was formulated for use with the pseudo-random spatial sampling of CYGNSS. This method derives historical relationships (here, we used data from 2017 to 2018) between observations of  $\Gamma$  in nearby grid cells and then applies these relationships to future, unobserved values of  $\Gamma$ . More simply, we calculate the linear relationship between reflectivity in one grid cell and reflectivity in a neighboring grid cell. If there is a future value of reflectivity in one grid cell but not the other, then the linear relationship can be used to estimate the reflectivity in the un-observed grid cell. This method better preserves the highly spatially heterogeneous nature of  $\Gamma$  observations than do other interpolation methods, and POBI has been shown to recreate truth observations with relatively low errors of  $0.17 \pm 1.96$  dB (Chew, 2021). However, it is not known how well the interpolation method performs in situations where inundated areas no longer follow historical patterns, as is often the case with floods with return intervals longer than the training dataset. We hypothesize that POBI performs better in regions that undergo regular and expected changes in inundation extent and will not work as well in regions experiencing flooding that was not also experienced during the time interval used for the creation of the neighbor relationships. We will assess this aspect of the POBI method

**Box 1**  
Inundation reflectivity model.



The model used for retrieving the inundated grid cell fraction is described and corroborated in *Chew and Small (2020b)*. This is just a brief summary; for further details, please see the aforementioned paper. The model assumes that the observed reflectivity can be approximated as a weighted average of the reflectivity of the inundated and un-inundated grid cell fractions, with the weights determined by their respective grid cell fractions:

$$\Gamma_{\text{surface}} = \rho \times \Gamma_{\text{inundated}} + (1 - \rho) \times \Gamma_{\text{dry}} \quad (2)$$

$\Gamma_{\text{surface}}$ : reflectivity of the cell (what we observe)  
 $\rho$ : the inundated fraction of the cell (what we want to retrieve)  
 $\Gamma_{\text{inundated}}$ : reflectivity of the water  
 $\Gamma_{\text{dry}}$ : reflectivity of the un-inundated portion of the cell  
 (what we must estimate)

In order to estimate  $\Gamma_{\text{inundated}}$  and  $\Gamma_{\text{dry}}$ , we can use the following equations:  
 (terms in blue are ancillary data or parameters)

$$\Gamma_{\text{inundated or dry}} = 10 \log_{10} |\Gamma_{\text{lhcp,rough}}|^2 \quad (3)$$

$$\Gamma_{\text{lhcp,rough}} = S_r \times \Gamma_{\text{lhcp}} \quad (4)$$

$$\Gamma_{\text{lhcp}} = 0.5(r_v - r_h) \quad (5) \quad S_r = \exp(-2[2\pi\sigma \cos \theta/\lambda]^2) \quad (6)$$

$$\Gamma_h = \frac{\sqrt{\epsilon_{\text{air}} - \sin^2 \theta} - \sqrt{\epsilon_{\text{surface}} - \sin^2 \theta}}{\sqrt{\epsilon_{\text{air}} - \sin^2 \theta} + \sqrt{\epsilon_{\text{surface}} - \sin^2 \theta}} \quad (7)$$

$$\Gamma_v = \frac{\epsilon_{\text{surface}} \sqrt{\epsilon_{\text{air}} - \sin^2 \theta} - \epsilon_{\text{air}} \sqrt{\epsilon_{\text{surface}} - \sin^2 \theta}}{\epsilon_{\text{surface}} \sqrt{\epsilon_{\text{air}} - \sin^2 \theta} + \epsilon_{\text{air}} \sqrt{\epsilon_{\text{surface}} - \sin^2 \theta}} \quad (8)$$

$S_r$ : roughness of the surface  
 $\lambda$ : L1 wavelength  
 $\theta$ : incidence angle  
 $\sigma$ : RMS height of the surface, either soil ( $\sigma_{\text{soil}}$ ) or water ( $\sigma_{\text{water}}$ )

$\Gamma_{\text{lhcp,v,or h}}$ : reflection coefficient at LHCP, H, or V polarization  
 $\epsilon_{\text{air}}$ : dielectric constant of air (1.0)  
 $\epsilon_{\text{surface}}$ : dielectric constant of the surface, either water (78.9 + 4.3i (Kaatze, 1989)) or for soil with a given soil moisture value\*

\*The dielectric constant of soil is estimated using soil moisture and soil texture (Dobson et al., 1985; Hallikainen et al., 1985)

here. And, as is the case with all spatial interpolation methods, the further away in space from an observation of  $\Gamma$ , the more wary one should be of the interpolated value. Because POBI is an exact interpolator, which means observed values remain unchanged after interpolation, there is the choice to only use the observed cells in one's analysis if interpolated data are undesirable.

2.2. Reflectivity model

Thus far, research by the GNSS-R community has focused on two different pathways for producing inundation maps, both of which stem

from previous microwave radar and radiometer inundation mapping algorithms: thresholding the data to produce binary 'presence/absence' inundation maps (à la active radar), or using a continuous model function to produce fractional inundation maps (à la radiometers).

Here we use a continuous model function that relates observations of  $\Gamma$  to fractional inundation extent at the 3 km scale. Our continuous model function quantifies the relationship between  $\Gamma$  and fractional inundation extent, such that every observation of  $\Gamma$  can be used to infer inundation extent. The model (Chew and Small, 2020b) relates  $\Gamma$  to fractional inundation extent by assuming that the observed  $\Gamma$  is a weighted average of  $\Gamma$  coming from the inundated and un-inundated

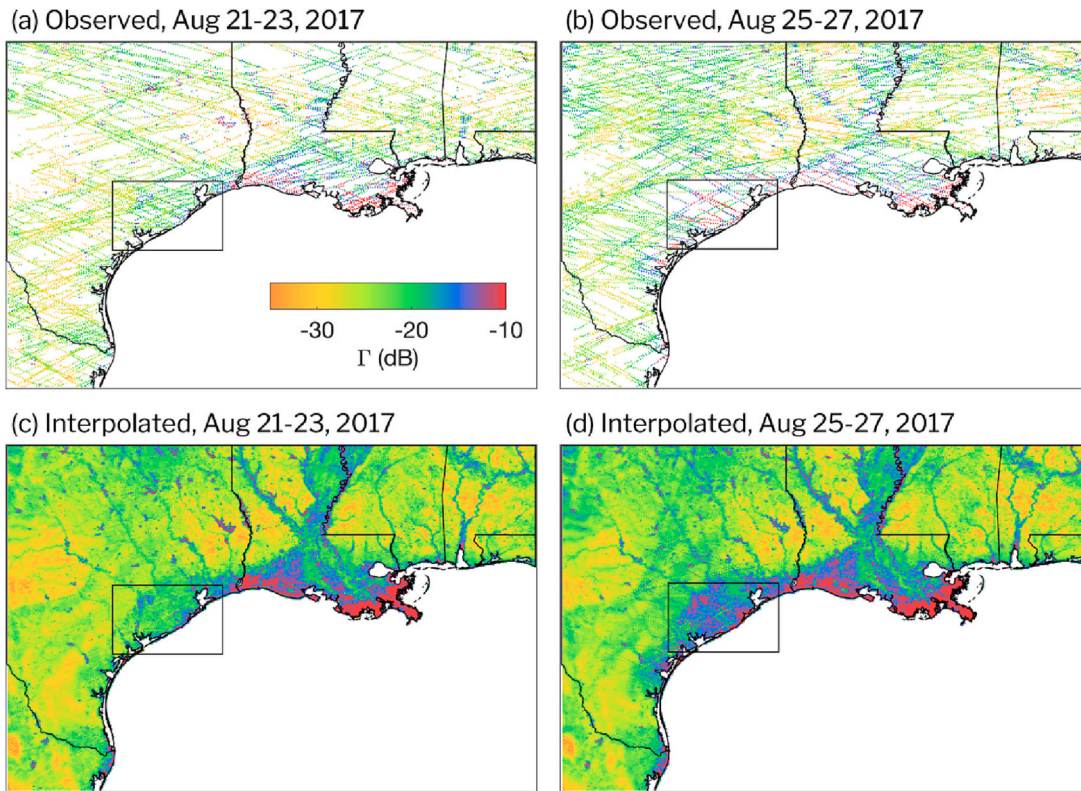


**Fig. 3.** 3-km gridded observations of  $\Gamma$  along the Texas and Louisiana coastlines between Aug 21–23, 2017 before Hurricane Harvey (a) and on August 25–27, 2017 after Hurricane Harvey (b). (c) and (d) are interpolated maps of  $\Gamma$  using the POBI method with (a) and (b), respectively. Black boxes indicate the region most affected by the flooding.

surfaces, with the weights being equal to their respective grid cell fractions. A similar weighted average approach was also applied to data from microwave radiometers in (Colosio et al., 2022). Although the aim of this work is not to re-describe what was presented in (Chew and Small, 2020b), Box 1 illustrates the equations and ancillary variables required by the model.

The relationship between  $\Gamma$  and fractional inundation depends on the characteristics of the reflecting surface. At a conceptual level, consider the case in which a topographically-rough desert is inundated. The  $\Gamma$  of the desert before the flood would be low while during the flood it would be high, leading to a large  $\Delta\Gamma$ . Alternatively, one could imagine a case where a previously saturated agricultural field is inundated. In this case, the  $\Gamma$  of the saturated field would be relatively high even before it flooded. Thus, the  $\Delta\Gamma$  would be smaller than in the case of the flooded desert.

In these conceptual examples, two landscapes devoid of surface water transitioned to completely flooded landscapes. But there are many scenarios in which the landscape only partially floods. We use a model to retrieve fractional inundation extent in order to account for competing landscape characteristics on  $\Gamma$  like soil moisture, land surface roughness, and the roughness of the water.

Fig. 4 illustrates the modeled effect of changing these three variables on the relationship between  $\Gamma$  and fractional inundation extent. When the un-inundated land surface is both dry and rougher than the water in the inundated grid cell fraction, the sensitivity of  $\Gamma$  to fractional inundation in that grid cell is the largest (pink line in Fig. 4). In this case, soil moisture of the un-inundated land surface has a negligible effect on  $\Gamma$ , which is why the pink and yellow lines are nearly perfectly overlapped in Fig. 4. Conversely, a perfectly smooth and saturated soil will actually produce higher  $\Gamma$  than if that same surface were flooded with rough water (black line): reflectivity decreases as inundation fraction increases. Smoother land surfaces, regardless of the roughness of water,

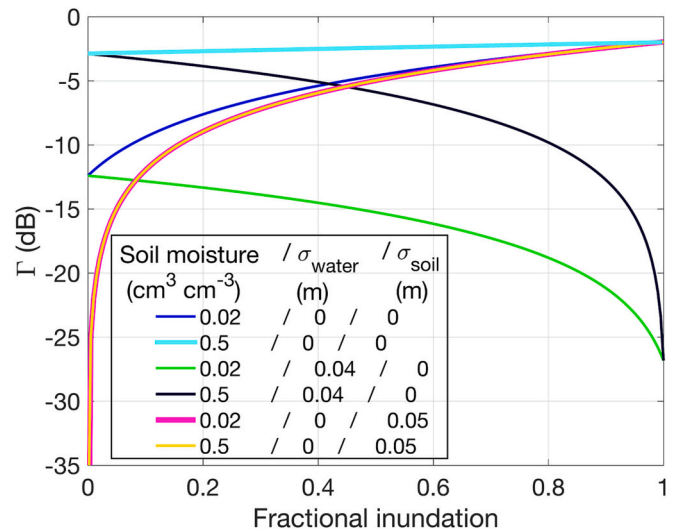


**Fig. 4.** Examples of end-member scenarios in the model. Each model simulation has a different combination of soil moisture, water roughness ( $\sigma_{\text{water}}$ ), and soil roughness ( $\sigma_{\text{soil}}$ ) parameters. All simulations were run assuming an incidence angle of 25 degrees and a loamy soil texture—varying the soil texture produces negligible differences in the model output.

require knowledge of soil moisture in order to understand how  $\Gamma$  varies with fractional inundation (e.g., the green vs. the black line in Fig. 4). This is why the roughness of the land and water surfaces as well as soil moisture must be estimated to retrieve inundation extent when using  $\Gamma$ . Later, we will show the differences in inundation retrievals that would result if these variables are ignored.

### 2.3. Model parameterization

What (Chew and Small, 2020b) did not do, and what we must do here, is estimate or parameterize soil moisture, surface roughness, the roughness of the water, and include the attenuating effect of vegetation such that we can retrieve inundation extent from any CYGNSS observation. We allow soil moisture to be both spatially and temporally variable, but both soil surface roughness and the roughness of water are assumed to be spatially variable but temporally static. Fig. 5 shows simplified flowcharts of both the parameterization and retrieval processes, the details of which are in the text below. Parameterization of the model and ultimate retrieval of inundation fraction requires ancillary datasets; although these are also described in the following text, we include a table in the Supplement summarizing the datasets as well (Table S1).

Ancillary datasets that describe soil surface roughness and the roughness of water at the spatial scale of CYGNSS do not exist. Thus, we inverted our reflectivity model to find the best fit values of soil surface and water roughness using calibration data or observations, all from the year 2018. For the case studies described in Section 3, we use observations from outside the calibration time period. In order to simplify model inversion, we used a data cube approach for both soil and water roughness parameterization (Table S1).

For the parameterization, we required a priori knowledge of where there might typically be surface water. To this end, we upscaled data from the Global Surface Water Explorer (GSWE) (Pekel et al., 2016), which is a 30-m global surface water dataset derived from Landsat data. We used GSWE data to quantify how many months out of the year (in 2018 only) surface water was present in each pixel. We considered any 30-m pixel with surface water presence >6 months out of the year to be semi-permanent water. We then calculated fractional inundation at the 3 km (CYGNSS) scale using the binary, 30-m semi-permanent water

mask. Because the GSWE is derived from optical data, it will underestimate the extent of semi-permanent water beneath vegetation canopies, which will affect our parameterization of water roughness in these pixels.

We now describe the methodology we used to parameterize the model. The general retrieval framework described here is flexible, and in the future these ancillary data sources and parameterizations could change as new and improved data become available.

#### 2.3.1. Soil texture

As shown in Box 1, soil texture is required by the model. However, the differences in the relationship between  $\Gamma$  and fractional inundation extent when we vary input soil texture are negligible. For all simulations and output we will show, we used a loamy soil texture as input.

#### 2.3.2. Vegetation

There is also no mention of vegetation in the model of (Chew and Small, 2020b), However, both modeling (Ferrazzoli et al., 2011; Pierdicca et al., 2014) and empirical (Carreno-Luengo et al., 2020) studies indicate that vegetation affects  $\Gamma$ . Despite these studies, relationships between  $\Gamma$  and vegetation characteristics are still relatively poorly understood or difficult to quantify due to a dearth of adequate observational data. Here, we assume that vegetation has an attenuating effect on  $\Gamma$  but does not change its sensitivity to surface water. In other words, ‘more’ vegetation will decrease  $\Gamma$  but not affect its relationship with fractional inundation extent (i.e., a curve in Fig. 4 retains its shape, but is shifted up or down).

We use an empirical relationship between  $\Gamma$  and a static dataset of above ground biomass (AGB) (Avitabile et al., 2016) to estimate the attenuating effect of vegetation on  $\Gamma$ . The AGB dataset has a native resolution of 0.01 deg., so we first upscaled the data to 3 km. First, we removed grid cells with 1% open water or greater, as indicated by the

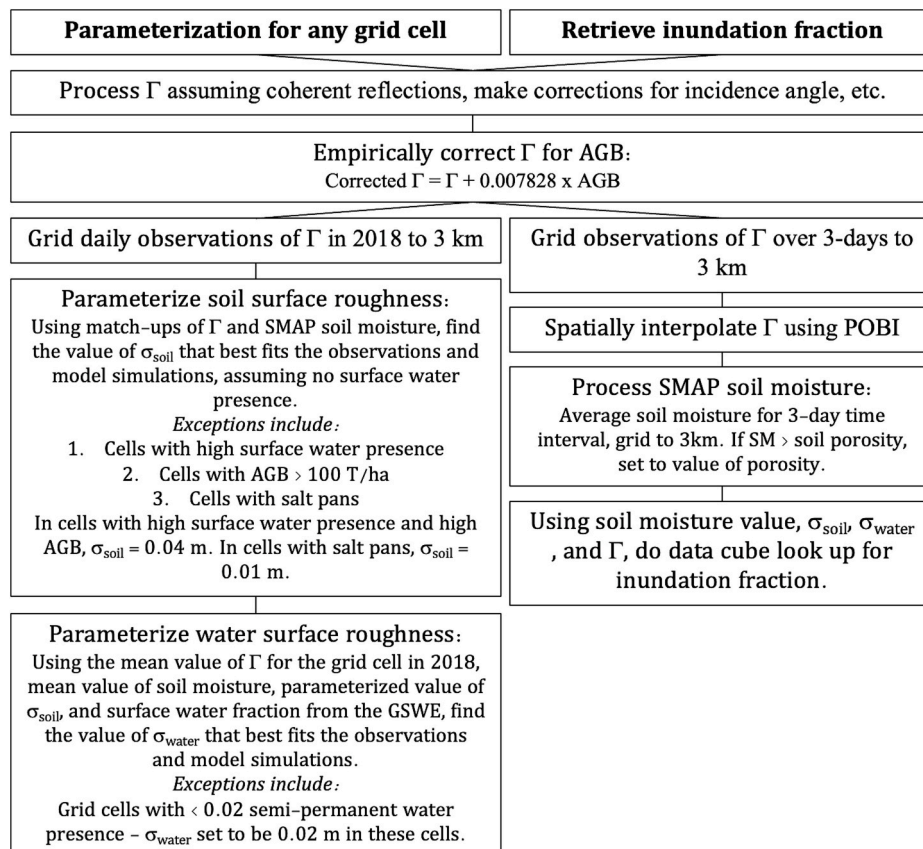


Fig. 5. Flowcharts illustrating the parameterization and retrieval processes.

Global Surface Water Explorer dataset. Then, we binned the upscaled biomass data by 5 T/ha and calculated the mean and standard deviation of  $\Gamma$  for these bins. We then calculated the regression coefficients for the best fit line between AGB and mean  $\Gamma$  and used this relationship to ‘correct’  $\Gamma$  for the effect of AGB. The correction was performed by adding the expected reduction in  $\Gamma$  due to AGB to the observed value of  $\Gamma$  (Fig. 6). The adjusted  $\Gamma$  was then used in the retrieval of inundation fraction and in the calibration of the model parameters. The correction shown in Fig. 6 is a simple one and does not consider how factors like seasonally-varying vegetation water content or canopy structure affect  $\Gamma$ . In the future, as our understanding of vegetation’s effect on  $\Gamma$  improves, we can update this correction as appropriate.

### 2.3.3. Soil surface roughness

The roughness of the land surface ( $\sigma_{\text{soil}}$ ), which here is defined as the root mean square (RMS) of the cm-level height deviations of the soil, is not well known. However, estimating the RMS surface height is important because rougher surfaces will lead to lower values of  $\Gamma$  for uninundated and partially-inundated land surfaces, which will affect how  $\Gamma$  changes as the surface floods, thus altering the overall shape of the curves in Fig. 4. There are several possible approaches for quantifying RMS surface heights. LIDAR surveys, usually done from aircraft, can provide cm-level height information. However, these data are sparsely available so it is not currently possible to map roughness from LIDAR for the entirety of CYGNSS’ coverage. Although digital elevation models (DEMs) are widely available, these data are too coarse to be used to quantify cm-level deviations. Other microwave missions like SMAP parameterize surface roughness based on land cover (O’Neill et al., 2018), but we have observed significant differences in  $\Gamma$  even within one land cover class. Thus, characterizing surface roughness based on land cover class is not sufficient for the GNSS-R scattering geometry.

Because of the above limitations, we parameterize soil surface roughness using collocated observations of  $\Gamma$  (observed and interpolated) and SMAP soil moisture (Enhanced Level 3 product (O’Neill et al., 2021)) from 2018, and then finding the modeled value of  $\sigma_{\text{soil}}$  (Box 1) that best fits the observed relationship. The outcome of this exercise is a gridded  $3 \times 3$  km static map of  $\sigma_{\text{soil}}$  that varies spatially. We used the 9 km gridded SMAP postings and downscaled them to 3 km by using the value in the closest 9 km grid cell to each 3 km cell. Only soil moisture retrievals that were less than the value of the soil porosity (Das and

O’Neill, 2020; Hengl et al., 2017) for that grid cell were considered to remove SMAP retrievals that can be affected by intermittent surface water. An example of the matchups for a location in west Texas is shown by the purple dots in Fig. 7. This location was chosen at random from a subset of matchups that had a correlation between reflectivity and soil moisture  $>0.7$ .

We compared these matchups to simulations from the model from Box 1 that were run assuming no surface water presence but with modeled  $\sigma_{\text{soil}}$  that varied between 0 and 0.05 m (colored lines in Fig. 7). We found the model simulation that best fit the observed relationship between  $\Gamma$  and soil moisture and used the best fit value of  $\sigma_{\text{soil}}$  for the static inputs of soil surface roughness in the inundation model. In Fig. 7, the black line shows the best fit model simulation for the observational matchups, which in this case is when  $\sigma_{\text{soil}} = 0.028$  m (RMSE = 1.7 dB).

Although in general the model fits to the observations were good (peak of the distribution of RMSE for all grid cells = 1.15 dB), there were exceptions:

1. Near rivers and lakes, where the SMAP soil moisture retrievals may be contaminated by surface water, the RMSE between the model and observations was more commonly  $>3$  dB.
2. Regions with AGB  $>100$  T/ha also exhibited worse model fits, which is  $<15\%$  of the CYGNSS-observed land areas.
3. Areas with salt pans (although only a small fraction of the CYGNSS sensing area,  $<0.27\%$ ) are known to produce erroneously high soil moisture retrievals and consequently resulted in poor model fits.
4. Grid cells in the Middle East, particularly around Syria, exhibited poor model fits due to known radio frequency interference (RFI).

For the above cases, with the exception of the cells likely affected by RFI, we did not use the best-fit modeled values of  $\sigma_{\text{soil}}$ . Instead, we set cells with significant semi-permanent water and cells with a high AGB to have high soil roughness values. For cells with a high AGB, we calculated the mean  $\Gamma$  for this group ( $-28.6$  dB), which corresponds to a modeled soil roughness of 0.04 m, and so we set all cells with a high AGB to have a soil roughness of 0.04 m. For cells with significant semi-permanent water, it was not possible to use this same approach, as mean  $\Gamma$  for this group is likely significantly influenced by the open water. For the time being, we set these cells to also have a soil roughness value of 0.04

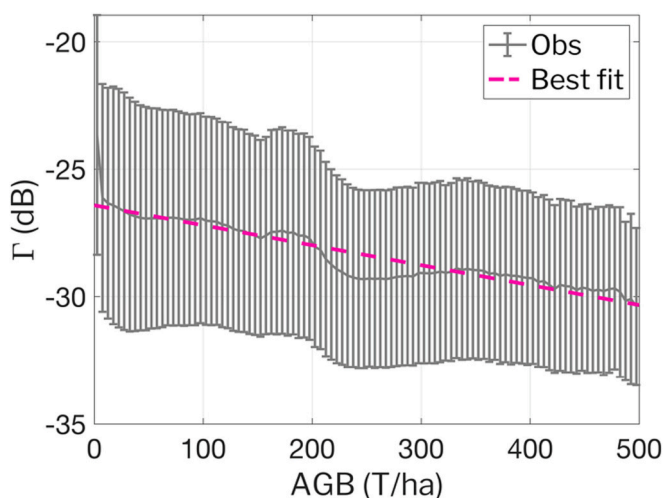


Fig. 6. The relationship between above ground biomass (AGB) and  $\Gamma$ , when AGB is binned in intervals of 5 T/ha. The mean is shown by the dark gray line, and the standard deviation is shown by the error bars. The pink dashed line is the best fit line to this relationship, where  $\Gamma = -0.007828 \times \text{AGB} - 26.42$ . (For interpretation of the references to color in this figure legend, the reader is referred to the web version of this article.)

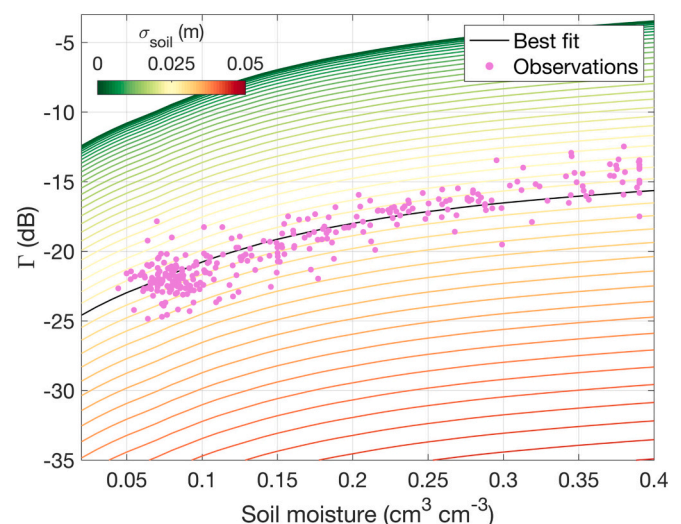
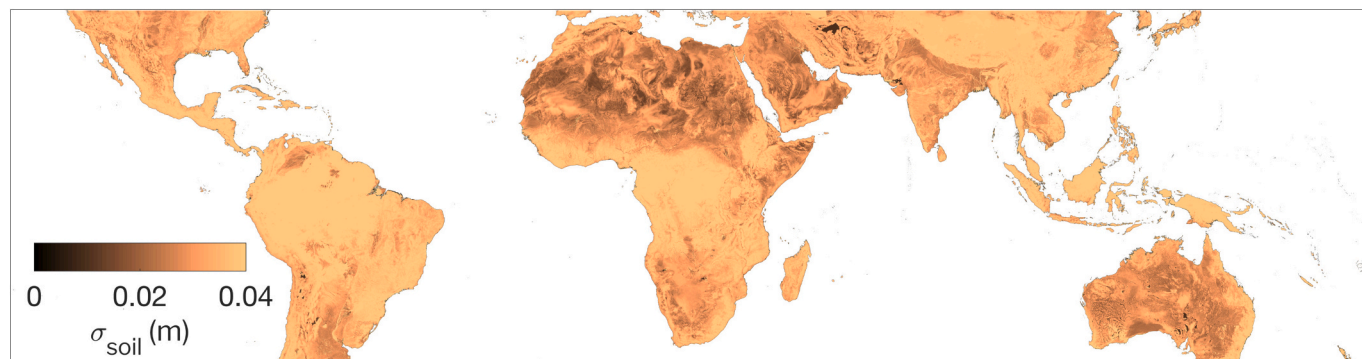


Fig. 7. The observed relationship between  $\Gamma$  and soil moisture in 2018 for one 3 km grid cell in Texas centered at 33.08 deg. N, 99.82 deg. W (purple dots). Colored lines are model simulations for this relationship with varying soil surface roughness. The black line is the best fit model simulation for the observations,  $\sigma_{\text{soil}} = 0.028$  m. (For interpretation of the references to color in this figure legend, the reader is referred to the web version of this article.)

**Table 1**  
Assigned values of  $\sigma_{\text{soil}}$  for categories of cells that exhibited poor model fits.

Category	Defined as	Assigned $\sigma_{\text{soil}}$
Cells contaminated by water	Cells with $>0.02$ semi-permanent water fraction in 2018, as indicated by the GSWE	0.04 m
Cells with high AGB	AGB $> 100$ T/ha	0.04 m
Salt pans	Cells falling within the boundaries of major salt pans (Patterson and Vaughn Kelso, 2022)	0.01 m



**Fig. 8.** Parameterized values of soil surface roughness ( $\sigma_{\text{soil}}$ ).

m, with the caveat that a different value could be used in future studies. Finally, for cells located in salt pans, we once again calculated the mean  $\Gamma$  for the group ( $-14$  dB), which corresponded to a soil roughness value of  $0.01$  m. These categories are defined and values of  $\sigma_{\text{soil}}$  described in Table 1.

Finally, in cells with no data, we used nearest neighbor interpolation to produce a spatially-complete map of parameterized  $\sigma_{\text{soil}}$ , which is shown in Fig. 8. Given the dearth of in situ soil roughness measurements, it is difficult to assess the global accuracy of the parameterizations, and our inability to separate soil surface roughness from large-scale topographic roughness conflates the two types of roughness in our parameterization. However, when we compared our value of  $\sigma_{\text{soil}}$  to in situ soil roughness measurements taken during a CYGNSS mission field campaign in Alamosa, CO, our value of  $0.027$  m was similar to those obtained during the field campaign, which ranged from  $0.007$  to  $0.0265$  m (Campbell et al., 2020).

#### 2.3.4. Water roughness

Assigning a temporally static value of water roughness ( $\sigma_{\text{water}}$ ) for any one grid cell is tricky, particularly for grid cells where historically there is not typically water. Water roughness depends on wind speed and the size of the water body. Larger water bodies tend to be deeper than smaller water bodies, and deeper water can accommodate larger waves. Larger water bodies are also less likely to be sheltered by surrounding vegetation. This introduces a somewhat circular problem: we need to know  $\sigma_{\text{water}}$  in order to retrieve surface water extent, but surface water extent in turn affects  $\sigma_{\text{water}}$ . This is exemplified in Fig. S2, which shows

our modeled values of  $\sigma_{\text{water}}$ , which we obtained by inverting the model to solve for  $\sigma_{\text{water}}$  given inputs of fractional inundation from the GSWE reference dataset, mean  $\Gamma$  and soil moisture for 2018, and parameterized surface roughness from Fig. 7. As surface water extent increases, so does  $\sigma_{\text{water}}$ . In grid cells that do contain semi-permanent water, this exercise can be used to parameterize  $\sigma_{\text{water}}$ , where  $\sigma_{\text{water}}$  for any particular grid cell is the output of  $\sigma_{\text{water}}$  inverted from the model (Fig. 9).

However, because here we are focused on flooding (i.e., retrieving surface water extent during times and in places where water is not typically found), we had to make a choice of how to parameterize  $\sigma_{\text{water}}$  in grid cells that are typically water-free (defined here as  $<0.02$  semi-permanent water as indicated by the GSWE). In these cells (white areas in Fig. 9), we assigned water roughness to be  $0.02$  m, which was the median retrieved water roughness value for cells with semi-permanent water presence.

The parameterized values of  $\sigma_{\text{water}}$  in Fig. 9 ignore the fact that this parameter can vary significantly over time, particularly over large bodies of water, due to temporal variations in roughening from wind. Future work could involve assigning realistic ranges to this parameter instead of one using one value, which could then provide reasonable uncertainty bounds on retrieved inundation fraction due to uncertainties in  $\sigma_{\text{water}}$ .

#### 2.3.5. Soil moisture

Unlike the parameterization of  $\sigma_{\text{soil}}$  and  $\sigma_{\text{water}}$ , the soil moisture input for the inundation retrieval is allowed to vary through time. Including an estimate of the soil moisture of the un-inundated cell fraction is

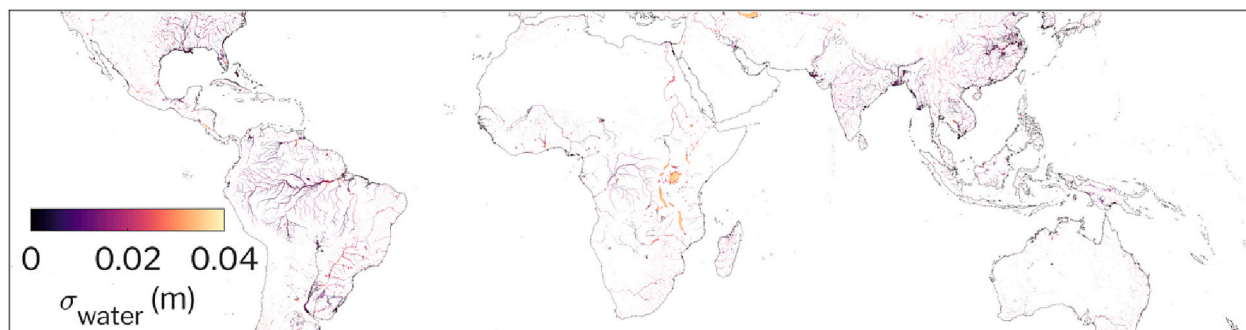


**Fig. 9.** Map of parameterized values of static water roughness  $\sigma_{\text{water}}$ . Inland grid cells without significant water ( $<0.02$  fractional coverage) in the calibration time period (cells in white) were set to have a  $\sigma_{\text{water}} = 0.02$  m.



important because  $\Gamma$  is affected by soil moisture. Without consideration of soil moisture, the algorithm would mistake fluctuations in  $\Gamma$  caused by soil moisture variations as fluctuations in inundation.

We use retrievals from the SMAP Level 3 Enhanced product for the soil moisture input (O'Neill et al., 2021). On any day X for a given grid cell, we use the most recent soil moisture retrieval, which can be from day X to day X-2, since the temporal repeat frequency of SMAP can be up to three days depending on latitude. We consider the soil porosity from the SMAP ancillary data (Das and O'Neill, 2020) in determining whether or not a soil moisture retrieval is above its saturated value and thus likely to be affected by transient water. If a soil moisture retrieval is higher than the value of its porosity, we set the soil moisture to be equal to the porosity, to represent the saturated soil moisture content. However, as we will show below, this threshold does not completely remove the effect of transient surface water on the soil moisture retrievals, and erroneously high soil moisture values tends to cause an underestimation of fractional inundation.

### 3. Inundation maps and sources of uncertainty

In this section, we compare CYGNSS-derived inundation maps to independent surface water maps from the Surface Water Microwave Product Series (SWAMPS) dataset, data from PALSAR-2 (Phased-Array L-band Synthetic Aperture Radar-2), flooding maps from the Dartmouth Flood Observatory (DFO), and the modified normalized difference water index (MNDWI) from MODIS, the Moderate Resolution Imaging Spectroradiometer. In some cases, we will show upscaled fractional inundation from the GSWE to compare with the 'before' or 'dry' inundation maps, as often it was difficult or impossible to find any cloud-free images from MODIS for the regions. When we upscale binary classifiers at high spatial resolution from PALSAR-2, the DFO, or MODIS, in all cases we do so by calculating the fraction of high-resolution cells within each 3 km cell that are classified as water and report that value as the upscaled inundation fraction.

First, we will describe the external surface water maps. Then, we will compare the maps with maps of inundation fraction derived from CYGNSS for several case studies, which were specifically chosen to highlight sources of uncertainty in the CYGNSS retrievals.

#### 3.1. Inundation dataset description and processing

##### 3.1.1. SWAMPS

The Surface Water Microwave Product Series (SWAMPS) is a gridded dataset of inundation fraction that is derived from data from several different high frequency microwave sensors, such as SSM/I SSMIS, ERS, QuikSCAT, and ASCAT (Jensen and McDonald, 2019). SWAMPS is one of the longest microwave remote sensing datasets available for download, and daily data files are available for the time period 2000–2020. The temporal repeat of the data is approximately 3 days, and the data are gridded to 25 km.

##### 3.1.2. PALSAR-2

PALSAR-2 is an L-band monostatic radar onboard the ALOS-2 satellite, which was launched by the Japanese Space Agency in 2014. Although the data have a very high spatial resolution (25 m) and can penetrate denser vegetation than any other ancillary dataset we describe here, there are only a very limited amount of data that are publicly available. Here, we use PALSAR-2 data from an annual mosaic that have been radiometrically balanced and georectified for the year 2019 (JAXA, 2022).

We specifically use PALSAR-2 data to identify regions of open water and flooded forest in the Amazon, so we use HH polarization backscatter data in our analysis, as HH polarization has been shown to be more sensitive to double bounce scattering, which occurs in regions of dense, flooded vegetation (Rosenqvist et al., 2020). In order to create an analogous 3 km map of inundation fraction from the PALSAR-2 data, we

first thresholded the data to identify pixels that were likely dry forest, open water, and flooded forest (see the Supplement for more details on the distribution of the data and thresholding). From this we created a binary classifier, where dry forest was considered one class and open water and flooded forest were grouped together as the other class. We then upscaled the binary, 25 m map to a 3 km map of inundation fraction, which we could then directly compare to the CYGNSS data.

##### 3.1.3. Dartmouth flood observatory

Flooding maps produced by the Dartmouth Flood Observatory are often an aggregation of multiple data sources, many of them optical. Here, we use maximum observed flooding produced by the DFO for Cyclone Idai in Malawi. For this event, the DFO map is primarily comprised of data produced by the Atmospheric Environmental Research, Inc. (AER), which used a downscaling algorithm on coarse-scale (22 km) microwave data to produce a 90 m spatial resolution map. The final map produced by the DFO also contained data from MODIS (data downloaded from <https://floodobservatory.colorado.edu/Events/4725/2019Malawi4725.html>).

##### 3.1.4. MNDWI from MODIS

Our MODIS surface water maps were derived by thresholding MNDWI from the MODIS/Terra Surface Reflectance Daily 500 m product. MNDWI is calculated using a ratio between Bands 4 (Green) and 6 (shortwave infrared) (Xu, 2006):

$$MNDWI = \frac{Band\ 4 - Band\ 6}{Band\ 4 + Band\ 6} \quad (S1)$$

After we calculated MNDWI and georeferenced the scene, we removed cloud and cloud-adjacent cells using the cloud mask contained in the MODIS product. We then imposed a threshold such that MNDWI  $\geq 0$  was set to be water, which is the standard threshold (Xu, 2006). After doing so, we were left with a 500 m binary map of surface water presence, which we upscaled to the 3 km gridding scheme of CYGNSS and determined fractional inundation.

##### 3.1.5. CYGNSS

For all CYGNSS inundation maps, we used the parameterized values of soil surface and water roughness, concurrent soil moisture retrievals from SMAP, and interpolated reflectivity observations to retrieve fractional inundation. We show both before and after flood inundation maps using CYGNSS data. In most figures, we overlay our data over shaded relief maps for context.

#### 3.2. Case studies

We discuss four case studies to compare our inundation maps with datasets from other sensors and to highlight specific sources of uncertainty in the retrievals. These example maps will give users of the fractional inundation product a better understanding of error sources and a greater context for its utility. Tables S3–6 summarize the statistical comparisons discussed for each of the case studies. In each case study, we focus on different specific sources of uncertainty. However, all sources of uncertainty discussed affect the retrieved inundation in each of the four examples to varying degrees. There are several broad categories of uncertainty that lead to differences between our inundation maps and ancillary data sources:

1. Uncertainty in the reflectivity observation due to calibration errors, gridding, and spatial interpolation.
2. Uncertainty due to inaccurate model parameterization and ancillary data.
3. Uncertainty in the external inundation maps themselves.

### 3.2.1. The Amazon

Our first case study compares maps of inundation fraction from CYGNSS to both the SWAMPS dataset and data from PALSAR-2. Here, we illustrate retrieved inundation extent in regions of flooded forests as well as open water. Fig. 10a shows CYGNSS inundation fraction for the month of May 2019, for a large region within the Amazon basin. The Amazon encompasses areas of dense tropical forest, open water, and flooded forest.

In order to understand the performance of the algorithm in regions of flooded forest, we compared the CYGNSS maps in the Amazon to maps of inundation fraction from a PALSAR-2 tile (shown by the boxes in Fig. 10a), which we created by manually thresholding the HH backscatter data and then upscaling to 3 km (see Supplement for further details). Because the PALSAR-2 tile we chose is a mosaic of data sampled from April 30, May 9, and May 23, 2019, we chose to compare the PALSAR-2 data to the mean CYGNSS inundation map for the entire month of May of that year (Fig. 10a).

Fig. 11a shows a zoomed in view of the mean CYGNSS inundation fraction for May 2019 for the extent of the PALSAR-2 tile (extent outlined by the black box in Fig. 10a). There are regions of high, medium, and low inundation extent in this image. Fig. 11b shows the corresponding upscaled map of inundation fraction derived from PALSAR-2, and the difference between the CYGNSS and PALSAR-2 maps of inundation fraction are shown in Fig. 11c. In this panel, red pixels are where PALSAR-2 indicated more surface water, and blue pixels are where CYGNSS indicated more surface water. The scatter plot in Fig. 11d shows the relationship between CYGNSS and PALSAR-2 inundation fraction for this tile. In general, both CYGNSS and PALSAR-2 retrieve very similar levels of inundation fraction, with a root mean square difference (RMSD) of 0.07 and an  $r^2$  of 0.91. However, we can also see from the best fit relationship between CYGNSS and PALSAR-2 (solid black line in Fig. 11d), that the CYGNSS algorithm does underestimate inundation fraction in pixels with high surface water extents, which tend to be in areas of open water, though not always. Our algorithm also tends to underestimate the inundation fraction in regions of flooded forest (regions of high backscatter in Fig. S3a). Including a more advanced consideration for the attenuation of vegetation on reflectivity than we do here will be the subject of future research.

We also compared the CYGNSS inundation fraction data in this location to inundation fraction in the SWAMPS dataset. Because the SWAMPS dataset contains daily retrievals on a 25 km grid (though the actual temporal repeat in any one location is between 3 and 5 days), we can compare time series of CYGNSS and SWAMPS.

Fig. 12a shows time series of mean inundation fraction for the same region as the PALSAR-2 tile (black box in Fig. 10a) for SWAMPS (red dots) and CYGNSS (black dots) for 2018–2020. There is a noticeable bias between the two datasets, with the SWAMPS data showing approximately 0.04 higher inundation fraction than CYGNSS. The SWAMPS data are also higher than the mean value of inundation fraction from PALSAR-2 (blue dot in Fig. 12a). The bias might be due to the fact that the SWAMPS data, given their 25 km resolution, are not perfectly confined to the region of interest and will be influenced from water outside of the tile. When the bias is removed relative to the CYGNSS data (Fig. 12b), it is easier to see the similarities in seasonal variations in the datasets—both CYGNSS and SWAMPS show very similar timings of annual maximums and minima as well as amplitudes of seasonal changes and day-to-day scatter. A scatter plot of the CYGNSS and SWAMPS retrievals for the region are shown in Fig. 12c. Day-to-day scatter in CYGNSS retrievals is due to a combination of factors that we illustrate in this manuscript: temporal variations in water roughness, uncertainties in the  $\Gamma$  observations, and errors and uncertainties in the interpolation scheme.

We can also upscale the CYGNSS inundation retrievals to illustrate how SWAMPS and CYGNSS compare regionally, which we show in Fig. 10b,c. Fig. 10b shows mean inundation fraction from SWAMPS for May 2019, and Fig. 10c shows the mean inundation fraction from

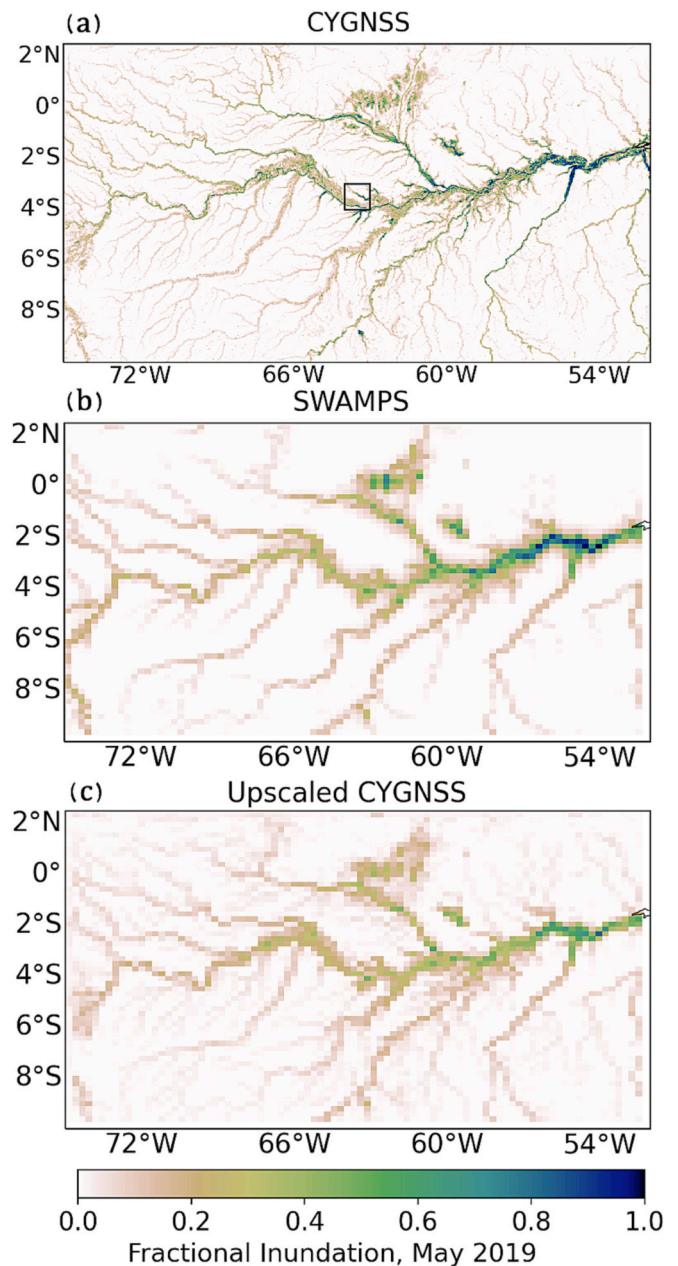
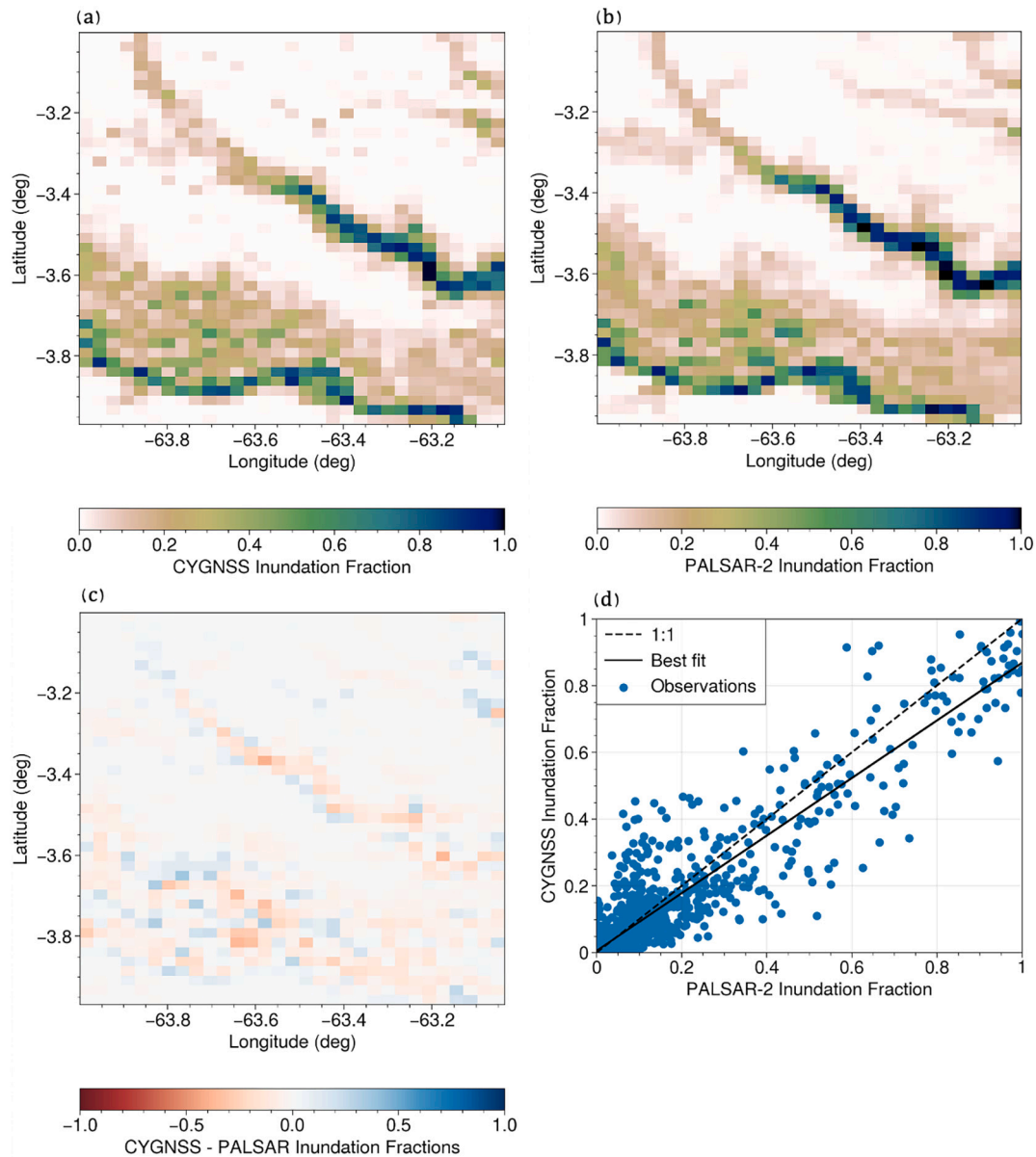


Fig. 10. Mean inundation fraction for May 2019 over the Amazon Basin from CYGNSS (a) and SWAMPS (b). (c) is an upscaled version of (a), which has been gridded to the same resolution of SWAMPS.

CYGNSS, after upscaling the 3 km data to 25 km. There is broad spatial agreement between the two datasets. However, relative to SWAMPS, CYGNSS underestimates inundation fraction in grid cells with a large surface water extent, though the CYGNSS map also retrieves a larger amount of surface water in regions of low inundation extent, which is possibly related to the higher native spatial resolution of the CYGNSS data relative to SWAMPS.

The underestimation of CYGNSS inundation fraction over regions with a large extent of open water could be indicative of the parameterized values of  $\sigma_{\text{water}}$  being too low in this region, either generally or specifically for this time period, or it is possible that SWAMPS is overestimating inundation fraction. Although we did not incorporate temporally-varying values of  $\sigma_{\text{water}}$ , further investigation into modeling their expected variations could be useful in providing better estimations of upper- and lower-bounds of retrieved inundation extent. In the



**Fig. 11.** Mean inundation fraction for May 2019 from CYGNSS (a) and PALSAR-2 (b). The difference between the two are shown in (c), and their relationship on a pixel-by-pixel basis is shown (d).

current version of our data product, however, users should be cognizant of this expected underestimation with respect to SWAMPS.

### 3.2.2. Mozambique, cyclone Idai 2019

Cyclone Idai caused severe flooding along the coastline of Mozambique in March 2019. For this example, we do not display MODIS-based inundation from before the event, as cloud-free images were not available. This event was significant enough to activate flood inundation mapping from the DFO. DFO flood maps are typically derived from an aggregation of downscaled or high-resolution remote sensing data and observations and represent all retrieved inundation for the event (Brakenridge and Karnes, 1996). As such, comparison flood maps from the DFO do not characterize inundation for a particular time, but the maximum extent of flooding throughout the event. The CYGNSS inundation maps have a temporal resolution of three days. To compare with DFO, we aggregated the post-Cyclone Idai CYGNSS inundation map to represent the maximum extent of flooding that we retrieved over the time period.

Relative to semi-permanent water extent in the area (Fig. 13a), the DFO mapped extensive flooding due to Cyclone Idai (Fig. 13b). CYGNSS inundation maps from before (Feb 25–27, 2019) and after (using an aggregation of data between March 11–26, 2019) Cyclone Idai are shown in Fig. 13 (c,d), which also show a significant increase in fractional inundation. Many grid cells in Fig. 13d show complete inundation, and inundation extent increased along the Zambezi River relative to Fig. 13c. Semi-permanent water from the GSWE shows very similar fractional inundation for the reservoir and Zambezi River as the ‘before’ CYGNSS image (Fig. 13c). There are some differences along the coastline, with the CYGNSS inundation map showing greater inundation extent than the GSWE, though because the GSWE is from 2018, the two time periods do not overlap.

Similar spatial patterns of maximum inundation extent exist between the DFO map (Fig. 13b) and that retrieved by CYGNSS (Fig. 13d). However, the DFO map shows higher fractional inundation values, and the inundation is more concentrated in specific areas. This is in contrast to the CYGNSS map, which shows increased moderate fractional

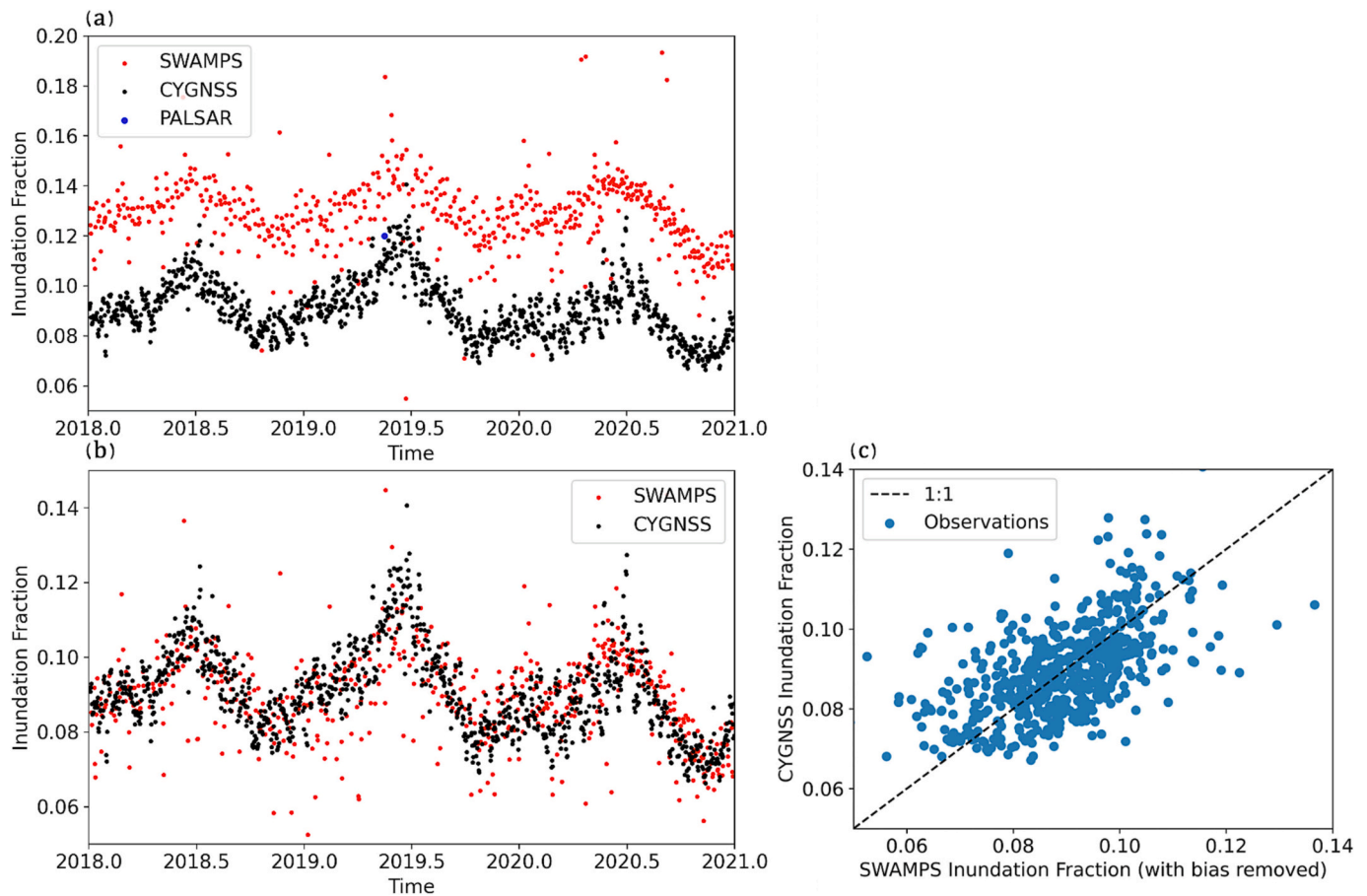


**Fig. 12.** (a) Inundation fraction for the region outlined in the black box in Fig. 10a for SWAMPS (red dots), CYGNSS (black dots), and the mean value for May 2019 for the PALSAR-2 tile (blue dot). (b). Same as (a), but with the SWAMPS data debiased relative to CYGNSS. (c) Scatter plot of the de-biased SWAMPS and CYGNSS retrieved values of inundation fraction shown in (b). Note that the axes are constrained in this panel. Constraining the axes removes a few outliers in the SWAMPS time series, which are due to the fact that, occasionally, the region of interest was only partially sampled by the sensors used in the SWAMPS retrievals. (For interpretation of the references to color in this figure legend, the reader is referred to the web version of this article.)

inundation in the two regions indicated by arrows in Fig. 13. This could be due to the fact that the DFO map was created in large part by downscaling a radiometer product through the use of a digital elevation model (DEM), which might tend to put more water in channels and low-lying areas.

If the DFO map is used as truth, then the CYGNSS inundation map on average underestimates fractional inundation by 0.06, with an RMSD of 0.16 (Table S4). We now discuss several possible reasons why our maximum inundation map from Cyclone Idai underestimates fractional inundation relative to the DFO map.

**3.2.2.1. Uncertainty in reflectivity observations.** Uncertainties in the CYGNSS observations themselves introduce uncertainties into our maps of fractional inundation. We estimate the uncertainty in the  $\Gamma$  observations (neglecting uncertainty in the interpolation process) to be  $\pm 1.74$  dB (Supplement), a large fraction of which is likely due to the switch of many GPS satellites to ‘flex power mode’ in February 2020 (Wang et al., 2019). This, along with other uncertainties stemming from the fact that CYGNSS data are not calibrated for land surface remote sensing, can cause both random noise and also entire CYGNSS tracks that are biased up or down relative to surrounding tracks.

The uncertainty in  $\Gamma$  leads to uncertainty in the inundation retrievals, and because the relationship between  $\Gamma$  and fractional inundation is not linear (i.e., Fig. 4), this does not translate to a simple bulk characterization of uncertainty in the inundation retrievals. However, we can create upper- and lower-bounds on the inundation retrievals using our estimate of the uncertainty in  $\Gamma$ . Examples of lower- and upper-bounds of

inundation based on the uncertainty in  $\Gamma$  alone are shown in Fig. 13e,f. These inundation maps were created using the same soil moisture retrievals and parameterizations of  $\sigma_{\text{soil}}$  and  $\sigma_{\text{water}}$ , but we varied the  $\Gamma$  by  $\pm 1.74$  dB to create upper- and lower-bounds of fractional inundation. As shown in Fig. 13e,f, the range of inundation that could result from this uncertainty is large and tends to be most significant in regions where inundation fraction is  $> 0.5$ . This is due to the decreased sensitivity of reflectivity to changes in inundation fraction as inundation fraction (e.g., the flattening of the curves shown in Fig. 4 for high values of inundation fraction). In these cases, even small uncertainties in  $\Gamma$  can lead to differences in retrieved inundation fraction that can be  $> 0.3$ . Note that, for areas where inland water is expected to be more rough than the uninundated land surface (i.e., black and green lines in Fig. 4), we expect to see the opposite relationship, with larger uncertainty bounds found for lower values of inundation fraction. However, in most areas, parameterized values of water roughness is less than land surface roughness. As the calibration of the CYGNSS data over land improves in the future, we expect the associated uncertainty to decrease.

There is also a moderate amount of noise in the CYGNSS inundation maps in Fig. 13c,d that resembles speckle noise. The inundation maps have singular grid cells with very high retrieved inundation in mountainous regions that are not present in the external inundation maps in Fig. 13 a,b. When we look at the  $\Gamma$  grids in Fig. 14a,b, we see that  $\Gamma$  is very low throughout most of these areas, but the landscape is dotted with high  $\Gamma$ . These high  $\Gamma$  values cause the anomalously high fractional inundation. These singular grid cells are located in regions of complex terrain, which tend to produce lower-quality reflections close to our

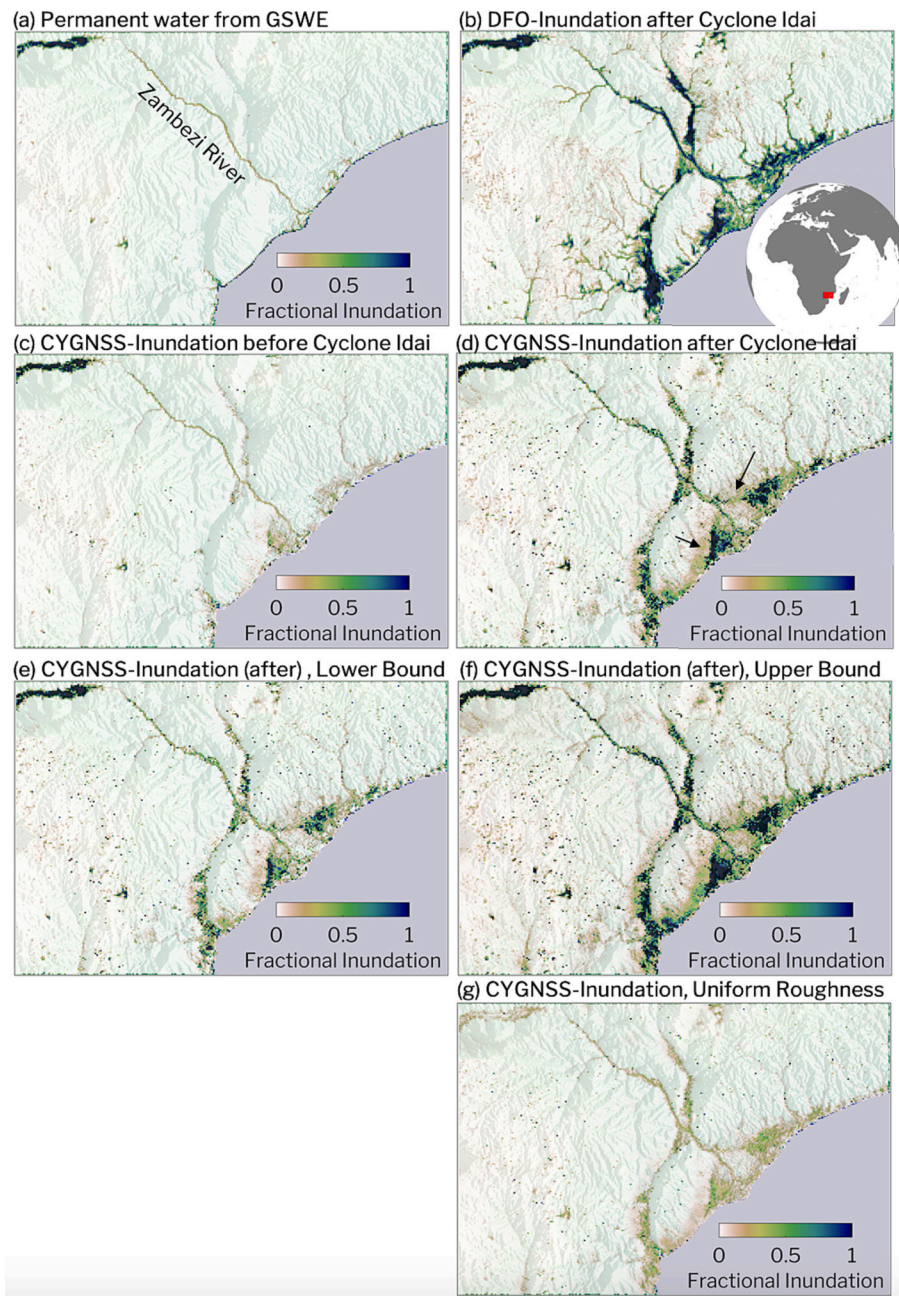


**Fig. 13.** (a) Reference semi-permanent water map from the GSWE. (b) Maximum flood extent mapped by the DFO. (c) CYGNSS inundation map before Cyclone Idai. (d) Maximum inundation mapped by CYGNSS after Cyclone Idai. (e) Lower-bound of maximum inundation fraction for CYGNSS, assuming uncertainty in reflectivity observations. (f) Upper-bound of maximum inundation fraction for CYGNSS, assuming uncertainty in reflectivity observations. (g) Maximum inundation fraction for CYGNSS if soil surface roughness were assumed to be 0.05 m and water roughness assumed to be 0 m.

signal-to-noise ratio (SNR) threshold of 2 dB. Improving data quality controls in the future could help reduce the amount of these anomalous grid cells. It is also possible that coarsening the grid cell size or using a longer time-averaging window than three days could also mitigate this issue. However, because our goal is to map inundation at relatively high spatiotemporal resolution, our resulting maps will contain more noise than monthly or seasonal maps.

**3.2.2.2. Uncertainties in model parameters and ancillary data.** Problems with soil moisture data for the un-inundated grid cell fraction introduce another source of uncertainty. SMAP soil moisture retrievals, and any satellite soil moisture retrieval, are themselves affected by surface water, with surface water presence introducing a high bias into the retrieved soil moisture value. Although we try to mitigate this effect by setting any soil moisture retrieval higher than the soil's porosity to be equal to the porosity, this will remain an issue. A high bias in the soil moisture retrieval could be one of the factors in the underestimation of fractional

inundation after Cyclone Idai, relative to the DFO. Fig. 14 shows all of the data or parameters required for the model retrieval for the CYGNSS inundation maps in Fig. 10. SMAP retrieved soil moisture  $>0.5 \text{ cm}^3$  for the majority of the coastline after Cyclone Idai (Fig. 14d), indicating that the retrievals were very likely biased by the presence of surface inundation. This bias can extend beyond just the grid cell affected by flooding, as the spatial resolution of the SMAP retrievals is  $>30 \times 30 \text{ km}$ , despite their posting to 9 km. Using too high of a soil moisture value in the model yields an underestimate of the fractional inundation for the grid cell, though quantifying these uncertainties is difficult, given that they will depend on the parameterizations of water and soil roughness (Fig. 4). However, if we were to ignore the effect of soil moisture on  $\Gamma$ , we would very often overestimate fractional inundation in regions not experiencing flooding and introduce false alarms into our inundation maps. We thus believe it is important to include soil moisture as an ancillary input to our inundation maps despite it leading to an underestimation of fractional inundation during a flooding event.

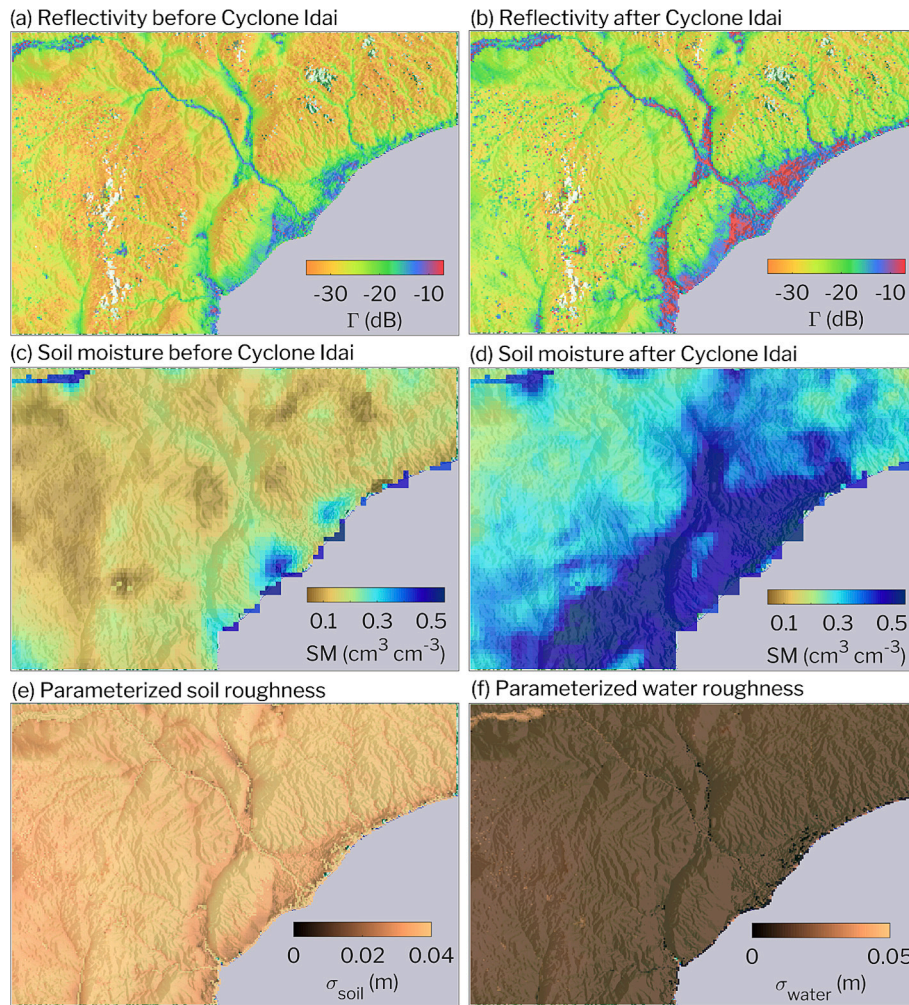


**Fig. 14.** Ancillary information required for the inundation retrieval from before (Feb 25–27, 2019, 1st column) and after (March 11–26, 2019, 2nd column) Cyclone Idai along the coast of Mozambique. Both soil roughness and water roughness are the same for before and after the event.

The parameterization of  $\sigma_{\text{soil}}$  reasonably fits the observed relationship between CYGNSS and SMAP. In contrast, one of the largest known unknowns is our parameterization of  $\sigma_{\text{water}}$ . Changing  $\sigma_{\text{water}}$  for a fully inundated surface from 0 to 0.04 m changes  $\Gamma$  by nearly 30 dB, which is almost the full range of observed values. Because there are no validation sources for  $\sigma_{\text{water}}$ , this is an uncertainty that users will have to contend with, and if the surface water is rougher than its parameterization value, CYGNSS will under-retrieve fractional inundation.

Given the uncertainty in soil moisture information and parameterization of  $\sigma_{\text{soil}}$  and considerable unknowns in  $\sigma_{\text{water}}$ , it is natural to wonder if including these parameters at all is worthwhile. Many microwave remote sensing retrieval algorithms for surface water mapping ignore the influence of soil moisture, and many other GNSS-R studies have assumed that the land surface is extremely rough and the inland water surface is perfectly smooth. Fig. 13g illustrates what would happen if we did not parameterize our model for these confounding factors. This figure shows maximum fractional inundation for Cyclone Idai if we assumed the soil surface to be rough ( $\sigma_{\text{soil}} = 0.05$  m, at this value the soil moisture influence is negligible) and the water surface to be perfectly smooth ( $\sigma_{\text{water}} = 0$  cm). Fractional inundation is vastly underestimated relative to inundation mapped by the DFO (Fig. 13b), with an RMSD of 0.2, which is for the most part caused by the assumption of a perfectly smooth water surface. Clearly, the inundation map produced by spatially-varying these parameters (Fig. 13d) is a significant improvement.

### 3.2.3. Mali, seasonal flooding 2020

Our third example is from the Inland Delta in Mali along the Niger River, which floods seasonally. False color images from MODIS from the dry and wet seasons are shown in Figs. 15a and b, respectively. A CYGNSS inundation map from the dry season (Fig. 15c) shows the Niger River as well as several small water features that dot the landscape. Visually, there is a good correspondence between the CYGNSS inundation map and the MODIS false color image from the dry season (Figs. 15a and c). The wet season CYGNSS inundation map from October 27–29, 2020 (Fig. 15d) shows higher fractional inundation than in April, notably in the Inland Delta. This same pattern is seen in the MODIS false color image in Fig. 15b. The October MODIS image also indicates there was a significant increase in active vegetation, in addition to the increased surface water.

*Uncertainty in external inundation maps:* Fig. 15 also shows SWAMPS inundation fraction maps in the same region for early April (e) and late October (f), 2020. In order to more easily compare the SWAMPS and CYGNSS inundation maps, we again upscaled our CYGNSS inundation retrievals to the same 25 km grid used by SWAMPS. The upscaled CYGNSS maps for April and October are shown in Fig. 15g and h, respectively. In this case, there are significant differences between the SWAMPS and CYGNSS maps. SWAMPS shows higher inundation fraction outside the Inland Delta in both April and October and lower inundation fraction within the Inland Delta in October. Given that the optical MODIS image does not show significant water outside of the Inland Delta, particularly in April, we believe that the CYGNSS retrievals

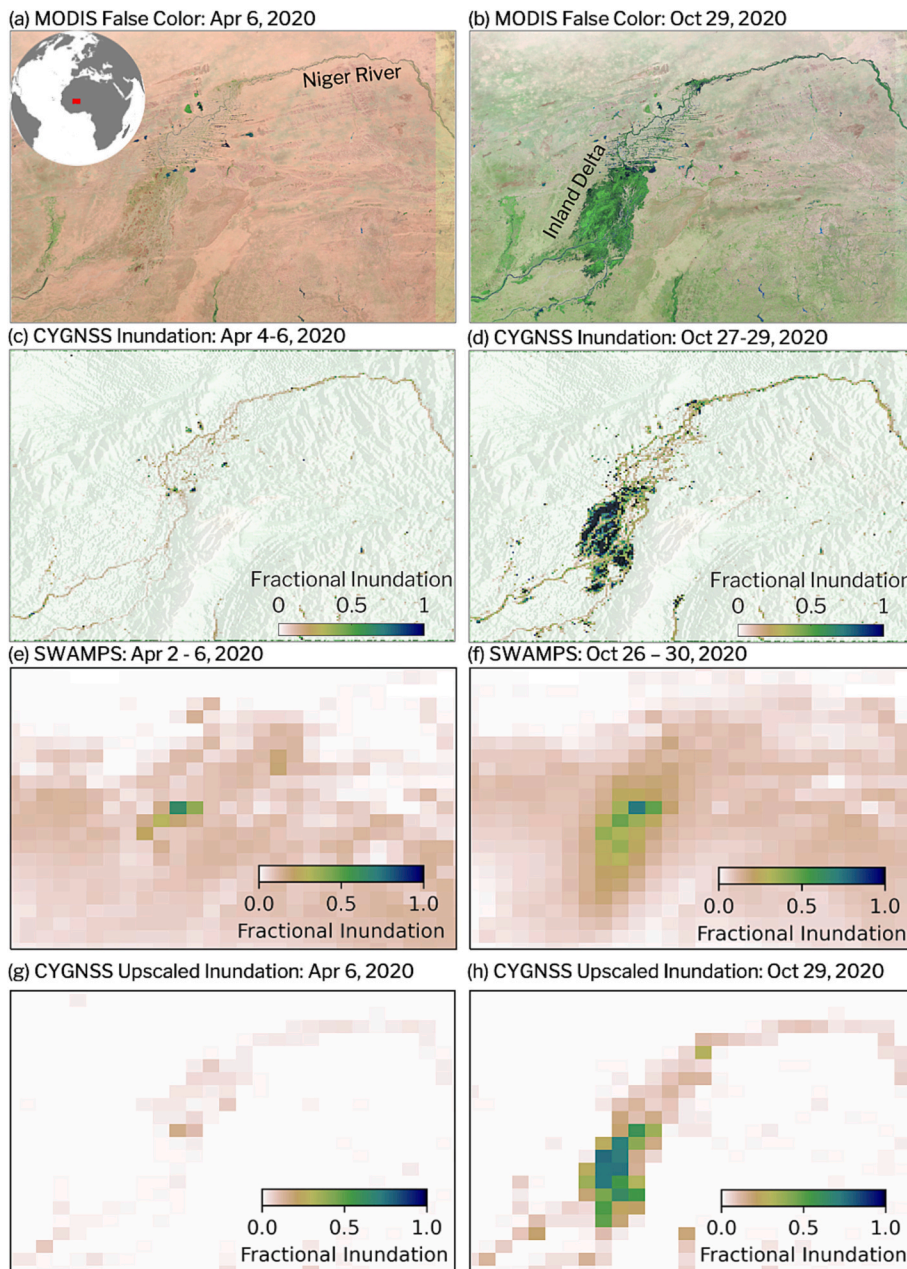


**Fig. 15.** (a) MODIS false color image recorded on Apr 6, 2020. The red box in the inset indicates the region represented by the maps. (b) MODIS false color image recorded on Oct 29, 2020. (c) CYGNSS inundation map derived from interpolated reflectivity observations recorded between Apr 4–6, 2020. (d) Same as (c), except using data between Oct 27–29, 2020. (e) Inundation map from SWAMPS (mean of retrievals Apr 2–6, 2020). (f) Same as (e), except for Oct 26 – Oct 29, 2020. (g) Same as (c), except upscaled to the same resolution of SWAMPS. (h) Same as (d), except upscaled to the same resolution of SWAMPS. (For interpretation of the references to color in this figure legend, the reader is referred to the web version of this article.)

may better represent the inundation extent in this particular case, and microwave radiometer retrievals of inundation fraction like SWAMPS are known to have issues in the Sahel. This example, along with the example over the Amazon, highlights the complementary nature of different sources of inundation information. Future work combining information from both CYGNSS and SWAMPS could take advantage of the relative merits of each dataset.

### 3.2.4. Australia, flooding 2019

Our fourth example comes from a region in Australia, which experienced significant flooding throughout Feb – Apr, 2019. Fig. 16a shows a CYGNSS fractional inundation map from before the flooding event (Jan 7–9, 2019). A comparison inundation map derived from MODIS is shown in Fig. 16c. Neither map shows significant inundation, and the RMSD between the two maps is 0.02.

Fig. 16b shows a CYGNSS inundation map from Apr 9–11, 2019, a time period during which the region was experiencing significant flooding. There are four distinct regions with increased inundation

relative to the inundation map from January. When we compare this map to a MODIS inundation map recorded for the same time period, we also see these four distinct flooded regions. However, fractional inundation is significantly less from CYGNSS than from MODIS, with an RMSD of 0.19. If only grid cells showing inundation in the CYGNSS map are considered, RMSD increases to 0.29.

*Uncertainties in the spatial interpolation:* Errors in spatial interpolation introduce error into the gridded  $\Gamma$  data and resulting inundation maps. This appears to be one of the driving factors behind the underestimation of fractional inundation in Fig. 16b. Fig. 17a shows the observed  $\Gamma$  grid that was spatially interpolated to create the complete  $\Gamma$  grid in Fig. 16b. Superimposed on the grids are three black ellipses, which we can track from the observed grid (Fig. 17a), to the interpolated grid (Fig. 17b), to the resulting inundation grid in Fig. 16b. The observed tracks within these ellipses show very high  $\Gamma > -10$  dB, and it is these cells that are producing the fractional inundation estimates of 1.0 that agree with the MODIS map in Fig. 16. Conversely, the interpolated cells over the flooded areas are closer to  $\sim -15$  dB (blue cells in Fig. 17b), which

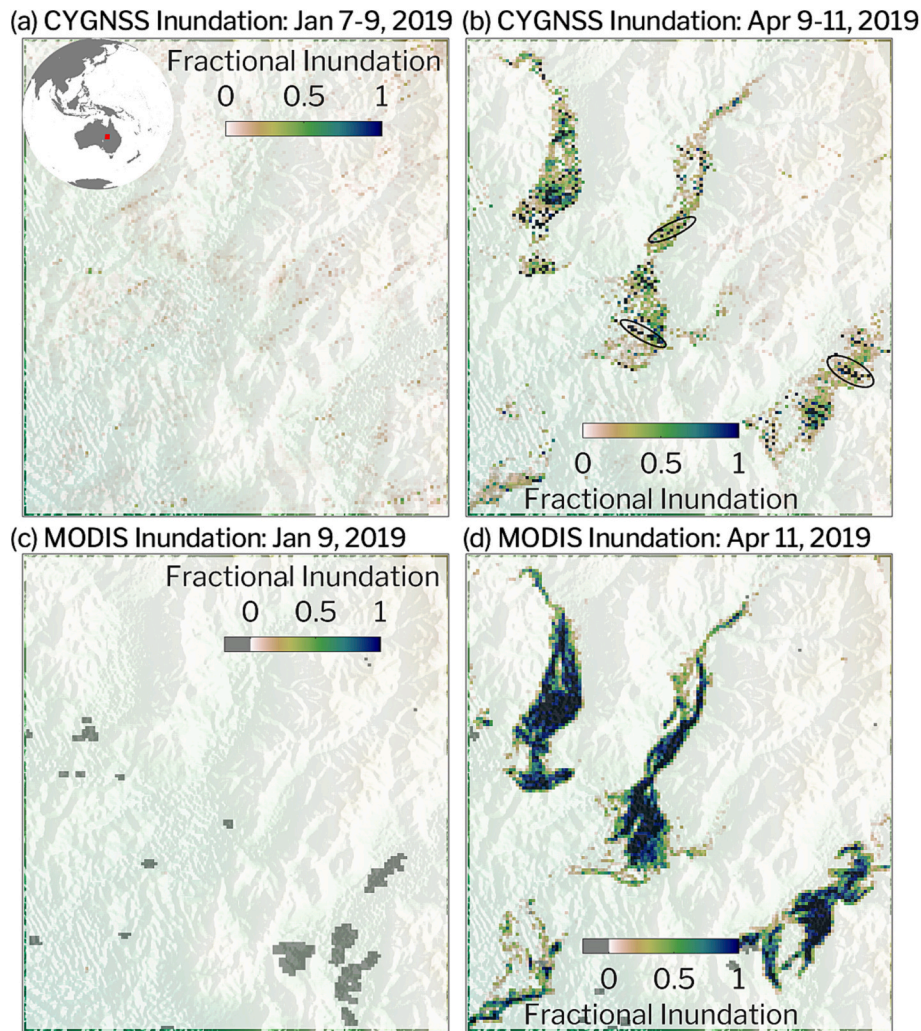


**Fig. 16.** (a) CYGNSS inundation map created using interpolated data recorded between Jan 7–9, 2019. (b) Same as (a), except for Apr 9–11, 2019. (c) MODIS inundation map for Jan 9, 2019. Pixels masked by clouds are shown in gray. (d) Same as (c), except for Apr 11, 2019. Black ellipses in (b) show three examples of non-interpolated tracks discussed in Fig. 17.

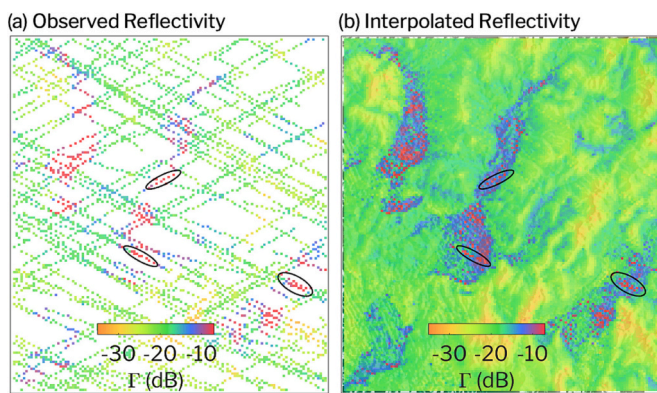


**Fig. 17.** (a) Observed reflectivity grid for Apr 9–11, 2019. Black ellipses show three sections of non-interpolated tracks discussed in the text. (b) Spatially-interpolated version of (a), which was used to derive results in Fig. 12b.

results in lower fractional inundation for these cells. If only observed cells were used to calculate the error between the CYGNSS inundation map and that from MODIS, then the RMSD would decrease from 0.19 to 0.12. It is clear that in this case, the POBI method did not perform

optimally, and future work is needed to adapt the method for these extreme events.

#### 4. Conclusion

This paper presented a retrieval algorithm for fractional inundation mapping using CYGNSS data as input to a parameterized reflectivity model. These maps are available at  $3 \times 3$  km resolution with a temporal resolution of three days for the entirety of CYGNSS' coverage ( $\pm 38$  deg. latitude). The CYGNSS inundation retrievals show similar seasonal changes in inundation extent over the Amazon as external inundation maps, and CYGNSS may outperform these maps in some regions. However, there are also several sources of uncertainty in the retrievals, two of which (parameterizations of soil moisture and water surface roughness) will tend to cause an underestimation of fractional inundation relative to other surface water products, particularly in regions with high surface water extent. Future work will focus on improving the parameterizations used in the model as well as adapting the spatial interpolation method to perform better during extreme events. Updating the input CYGNSS data to a newer version that accounts for temporally-varying GPS transmit power is also a high priority.



## CRedit authorship contribution statement

**Clara Chew:** Conceptualization, Methodology, Software, Validation, Formal analysis, Writing – original draft, Writing – review & editing, Visualization. **Eric Small:** Writing – original draft, Project administration, Funding acquisition. **Hannah Huelsing:** Data curation.

## Declaration of Competing Interest

The authors declare that they have no known competing financial interests or personal relationships that could have appeared to influence the work reported in this paper.

## Data availability

It is impossible to show all examples of flood inundation maps using this approach in one paper. We therefore encourage those interested in this method to go to: <https://data.cosmic.ucar.edu/gnss-r/inundation/cygnss/> in order to download additional CYGNSS flooding maps, which are currently available for the time period March 20, 2017 – June 30, 2022. We encourage caution when using the retrievals for hydrological analyses and for users to be aware of the uncertainties and shortcomings of the retrievals in their current form. Incorporating several sources of inundation maps into one's interpretation of inundation dynamics is likely to be more informative than using one source of data alone.

## Acknowledgements

This work was funded under the NASA Terrestrial Hydrology Program, award no. 80NSSC19K0046.

## Appendix A. Supplementary data

Supplementary data to this article can be found online at <https://doi.org/10.1016/j.rse.2023.113598>.

## References

- Al-Khaldi, M.M., Johnson, J., O'Brien, A., Balenzano, A., Mattia, F., 2019. Time-series retrieval of soil moisture using CYGNSS. *IEEE Trans. Geosci. Remote Sens.* 57, 4322–4331.
- Al-Khaldi, M.M., Shah, R., Chew, C., Johnson, J.T., Gleason, S., 2021. Mapping the dynamics of the south asian monsoon using CYGNSS's Level-1 signal coherency. *IEEE J. Sel. Top. Appl. Earth Obs. Remote Sens.* 14, 1111–1119.
- Avitabile, V., Herold, M., Heuvelink, G., Lewis, S.L., Phillips, O.L., Asner, G.P., 2016. An integrated pan-tropical biomass maps using multiple reference datasets. *Glob. Chang. Biol.* 22, 1406–1420.
- Baqir, M., Sobani, Z.A., Bhamani, A., Bham, N.S., Abid, S., Farook, J., Beg, M.A., 2012. Infectious diseases in the aftermath of monsoon flooding in Pakistan. *Asian Pac. J. Trop. Biomed.* 2, 76–79.
- Brakenridge, G.R., Karnes, D., 1996. The Dartmouth Flood Observatory: an electronic research tool and electronic archive for investigations of extreme flood events. In: Geological Society of America Annual Meeting. Geoscience Information Society Proceedings.
- Campbell, J., Melebari, A., Akbar, R., Moghaddam, M., 2020. Initial investigation of CYGNSS multiscale rough surface forward model at San Luis Valley Cal/Val Sites. In: CYGNSS Science Team Meeting. Pasadena, CA.
- Camps, A., Park, H., Pablos, M., Foti, G., Gommenginger, C.P., 2016. Sensitivity of GNSS-R spaceborne observations to soil moisture and vegetation. *IEEE J. Sel. Top. Appl. Earth Obs. Remote Sens.* 9, 4730–4742.
- Carreno-Luengo, H., Luzi, G., Crosetto, M., 2020. Above-ground biomass retrieval over tropical forests: a novel GNSS-R approach with CYGNSS. *Remote Sens.* 12, 1–29. <https://doi.org/10.3390/RS12091368>.
- Chapman, B.D., Russo, I.M., Galdi, C., Morris, M., Di Bisceglie, M., Zuffada, C., Downs, B., Lavalle, M., Loria, E., O'Brien, A., 2022. Comparison of SAR and CYGNSS surface water extent metrics. *IEEE J. Sel. Top. Appl. Earth Obs. Remote Sens.* 15, 3235–3245. <https://doi.org/10.1109/JSTARS.2022.3162764>.
- Chew, C., 2021. Spatial interpolation based on previously-observed behavior: a framework for interpolating spaceborne GNSS-R data from CYGNSS. *J. Spat. Sci.* <https://doi.org/10.1080/14498596.2021.1942253>.
- Chew, C., Reager, J.T., Small, E., 2018. CYGNSS data map flood inundation during the 2017 Atlantic hurricane season. *Sci. Rep.* 8 <https://doi.org/10.1038/s41598-018-27673-x>.
- Chew, C., Shah, R., Zuffada, C., Hajj, G., Masters, D., Mannucci, A.J., 2016. Demonstrating soil moisture remote sensing with observations from the UK TechDemoSat-1 satellite mission. *Geophys. Res. Lett.* 43 <https://doi.org/10.1002/2016GL068189>.
- Chew, C., Small, E., 2020a. Description of the UCAR/CU soil moisture product. *Remote Sens.* 12, 1558.
- Chew, C., Small, E., 2020b. Estimating inundation extent using CYGNSS data: a conceptual modeling study. *Remote Sens. Environ.* 246, 111869.
- Chew, C., Small, E., 2018. Soil moisture sensing using spaceborne GNSS reflections: comparison of CYGNSS reflectivity to SMAP soil moisture. *Geophys. Res. Lett.* 45, 4049–4057. <https://doi.org/10.1029/2018GL077905>.
- Clarizia, M.P., Pierdicca, N., Costantini, F., Floury, N., 2019. Analysis of CYGNSS data for soil moisture retrieval. *IEEE J. Sel. Top. Appl. Earth Obs. Remote Sens.* 12, 2227–2235. <https://doi.org/10.1109/JSTARS.2019.2895510>.
- Clarizia, M.P., Ruf, C., 2016. Wind speed retrieval algorithm for the cyclone global navigation satellite system (CYGNSS) Mission. *IEEE Trans. Geosci. Remote Sens.* 54, 4419–4432.
- Colosio, P., Tedesco, M., Tellman, E., 2022. Flood monitoring using enhanced resolution passive microwave data: a test case over Bangladesh. *Remote Sens.* 14 <https://doi.org/10.3390/rs14051180>.
- Das, N., O'Neill, P., 2020. SMAP Ancillary Data Report: Soil Attributes. Pasadena.
- De Roo, R.D., Ulaby, F.T., 1994. Bistatic specular scattering from rough dielectric surfaces. *IEEE Trans. Antennas Propag.* 42, 220–231. <https://doi.org/10.1109/8.277216>.
- Du, J., Kimball, J.S., Galantowicz, J., Kim, S.-B., Chan, S., Reichle, R., Jones, L., Watts, J., 2018. Assessing global surface water inundation dynamics using combined satellite information from SMAP, AMSR2 and landsat. *Remote Sens. Environ.* 213, 1–17.
- Durack, P.J., Wijffels, S.E., Matear, R.J., 2012. Ocean salinities reveal strong global water cycle intensification during 1950 to 2000. *Science* 336(6045), 455–458.
- Eroglu, O., Kurum, M., Boyd, D., Gurbuz, A.C., 2019. High spatio-temporal resolution cygnss soil moisture estimates using artificial neural networks. *Remote Sens.* 11 <https://doi.org/10.3390/rs11192272>.
- Ferrazzoli, P., Guerriero, L., Pierdicca, N., Rahmoune, R., 2011. Forest biomass monitoring with GNSS-R: theoretical simulations. *Adv. Space Res.* 47, 1823–1832. <https://doi.org/10.1016/j.asr.2010.04.025>.
- Gerlein-Safdi, C., Ruf, C., 2019. A CYGNSS-based algorithm for the detection of inland waterbodies. *Geophys. Res. Lett.* 46, 12065–12072.
- Gleason, S., Hodgart, S., Sun, Y., Gommenginger, C., Mackin, S., Adjrad, M., Unwin, M., 2005. Detection and processing of bistatically reflected GPS signals from low earth orbit for the purpose of ocean remote sensing. *IEEE Trans. Geosci. Remote Sens.* 43, 1229–1241. <https://doi.org/10.1109/TGRS.2005.845643>.
- Hengl, T., Mendes de Jesus, J., Heuvelink, G., Ruiperez Gonzalez, M., Kilibarda, M., Blagotic, A., Shangguan, W., Wright, M., Geng, X., Bauer-Marschallinger, B., Guevara, M.A., Vargas, R., MacMillan, R., Batjes, N., Leenaars, J., Ribeiro, E., Wheeler, I., Mantel, S., Kempen, B., 2017. SoilGrids250m: global gridded soil information based on machine learning. *PLoS One* 12, e0169748.
- JAXA, 2022. Global 25 m Resolution PALSAR-2 Mosaic (Ver.2.1.2) Dataset Description.
- Jensen, K., McDonald, K., 2019. Surface water microwave product series version 3: a near-real time and 25-year historical global inundated area fraction time series from active and passive microwave remote sensing. *IEEE Geosci. Remote Sens. Lett.* 16, 1402–1406. <https://doi.org/10.1109/LGRS.2019.2898779>.
- Kim, H., Lakshmi, V., 2018. Use of cyclone global navigation satellite system (CyGNSS) observations for estimation of soil moisture. *Geophys. Res. Lett.* 45, 8272–8282.
- Lefebvre, G., Davranche, A., Willm, L., Campagna, J., Redmond, L., Merle, C., Guelmami, A., Poulin, B., 2019. Introducing WIW for detecting the presence of water in wetlands with landsat and sentinel satellites. *Remote Sens.* 11, 10–14. <https://doi.org/10.3390/rs11192210>.
- Li, W., Cardellach, E., Ribó, S., Oliveras, S., Rius, A., 2022. Exploration of multi-Mission spaceborne GNSS-R raw IF data sets: processing, data products and potential applications. *Remote Sens.* 14, 1344. <https://doi.org/10.3390/rs14061344>.
- Li, W., Cardellach, E., Ribó, S., Rius, A., Zhou, B., 2021. First spaceborne demonstration of BeiDou-3 signals for GNSS reflectometry from CYGNSS constellation. *Chin. J. Aeronaut.* 34, 1–10. <https://doi.org/10.1016/j.cja.2020.11.016>.
- Melton, J.R., Wania, R., Hodson, E.L., Poulter, B., Ringeval, B., Spahni, R., Bohn, T., Avis, C.A., Beerling, D.J., Chen, G., Eliseev, A.V., Denisov, S.N., Hopcroft, P.O., Lettenmaier, D.P., Riley, W.J., Singarayer, J.S., Subin, Z.M., Tian, H., Zurcher, S., Brovkin, V., van Bodegom, P.M., Kleinen, T., Yu, Z.C., Kaplan, J.O., 2013. Present state of global wetland extent and wetland methane modelling: conclusions from a model inter-comparison project (WETCHIMP). *Biogeosciences* 10, 753–788. <https://doi.org/10.5194/bg-10-753-2013>.
- Morris, M., Chew, C., Reager, J.T., Shah, R., Zuffada, C., 2019. A novel approach to monitoring wetland dynamics using CYGNSS: Everglades case study. *Remote Sens. Environ.* 233, 111417.
- Muro, J., Canty, M., Conradsen, K., Huttich, C., Nielsen, A.A., Skriver, H., Remy, F., Strauch, A., Thonfeld, F., Menz, G., 2016. Short-term change detection in wetlands using Sentinel-1 time series. *Remote Sens.* 8, 795.
- Nakaegawa, T., 2012. Comparison of water-related land cover types in six 1-km global land cover datasets. *J. Hydrometeorol.* 13, 649–664. <https://doi.org/10.1175/JHM-D-10-05036.1>.
- O'Neill, P., Bindlish, R., Chan, S., Njoku, E., Jackson, T., 2018. Algorithm Theoretical Basis Document Level 2 & 3 Soil Moisture (Passive) Data Products.
- O'Neill, P.E., Chan, S., Njoku, E.G., Jackson, T., Bindlish, R., Chaubell, J., Colliander, A., 2021. SMAP Enhanced L3 Radiometer Global and Polar Grid Daily 9 km EASE-Grid Soil Moisture, Version 5..

- Patterson, T., Vaughn Kelso, N., 2022. Natural Earth Playas [WWW Document]. URL (accessed 1.1.22). <https://www.naturalearthdata.com/downloads/10m-physical-vectors/10m-playas/>.
- Pekel, J.-F., Cottam, A., Gorelick, N., Belward, A.S., 2016. High-resolution mapping of global surface water and its long-term changes. *Nature* 540, 418–422.
- Pierdicca, N., Guerriero, L., Giusto, R., Brogioni, M., Egido, A., 2014. SAVERS: a simulator of GNSS reflections from bare and vegetated soils. *IEEE Trans. Geosci. Remote Sens.* 52, 6542–6554. <https://doi.org/10.1109/TGRS.2013.2297572>.
- Prigent, C., Jimenez, C., Bousquet, P., 2020. Satellite-derived global surface water extent and dynamics over the last 25 years (GIEMS-2). *J. Geophys. Res. Atmos.* 125 <https://doi.org/10.1029/2019JD030711>.
- Prigent, C., Matthews, E., Aires, F., Rossow, W.B., 2001. Remote sensing of global wetland dynamics with multiple satellite data sets. *Geophys. Res. Lett.* 28, 4631–4634.
- Ringeval, B., de Noblet-Ducoudre, N., Ciais, P., Bousquet, P., Prigent, C., Papa, F., Rossow, W.B., 2010. An attempt to quantify the impact of changes in wetland extent on methane emissions on the seasonal and interannual time scales. *Glob. Biogeochem. Cycles* 24, GB2003.
- Rodriguez-Alvarez, N., Podest, E., Jensen, K., McDonald, K., 2019. Classifying inundation in a tropical wetlands complex with GNSS-R. *Remote Sens.* 11, 1053.
- Rosenqvist, J., Rosenqvist, A., Jensen, K., McDonald, K., 2020. Mapping of maximum and minimum inundation extents in the Amazon Basin 2014–2017 with ALOS-2 PALSAR-2 ScanSAR time-series data. *Remote Sens.* 12, 1326. <https://doi.org/10.3390/rs12081326>.
- Ruf, C., Unwin, M.S., Dickinson, J., Rose, R., Rose, D., Vincent, M., Lyons, A., 2013. CYGNSS: enabling the future of hurricane prediction. *IEEE Geosci. Remote Sens. Mag.* 1, 52–67.
- Schroeder, R., McDonald, K.C., Chapman, B.D., Jensen, K., Podest, E., Tessler, Z.D., Bohn, T.J., Zimmermann, R., 2015. Development and evaluation of a multi-year fractional surface water data set derived from active/passive microwave remote sensing data. *Remote Sens.* 7, 16688–16732.
- Senyurek, V., Lei, F., Boyd, D., Kurum, M., Gurbuz, A.C., Moorhead, R., 2020. Machine learning-based CYGNSS soil moisture estimates over ISMN sites in CONUS. *Remote Sens.* 12 <https://doi.org/10.3390/rs12071168>.
- Shindell, D.T., Walter, B.P., Faluvegi, G., 2004. Impacts of climate change on methane emissions from wetlands. *Geophys. Res. Lett.* 31.
- Tsyganskaya, V., Martinis, S., Marzahn, P., Ludwig, R., 2018. Detection of temporary flooded vegetation using Sentinel-1 time series data. *Remote Sens.* 10 <https://doi.org/10.3390/rs10081286>.
- Ulaby, F.T., Moore, R., Fung, A.K., 1986. *Microwave Remote Sensing, Volume 1: Fundamentals and Radiometry*. Artech House.
- Unwin, M.J., Pierdicca, N., Cardellach, E., Rautiainen, K., Foti, G., Blunt, P., Guerriero, L., Santi, E., Tossaint, M., 2021. An introduction to the HydroGNSS GNSS reflectometry remote sensing Mission. *IEEE J. Sel. Top. Appl. Earth Obs. Remote Sens.* 14, 6987–6999. <https://doi.org/10.1109/JSTARS.2021.3089550>.
- Wan, W., Liu, B., Zeng, Z., Chen, Xi, Wu, G., Xu, L., Chen, Xiuwan, Hong, Y., 2019. Using CYGNSS data to monitor China's flood inundation during typhoon and extreme precipitation events in 2017. *Remote Sens.* 11, 854.
- Wang, T., Ruf, C., Gleason, S., Block, B., McKague, D., O'Brien, A., 2019. A real-time EIRP level 1 calibration algorithm for the CYGNSS mission using the zenith measurements. In: *IGARSS 2019-2019 IEEE International Geoscience and Remote Sensing Symposium*. Yokohama, Japan, pp. 8725–8728.
- Xu, H., 2006. Modification of normalised difference water index (NDWI) to enhance open water features in remotely sensed imagery. *Int. J. Remote Sens.* 27, 3025–3033.
- Yan, Q., Huang, W., Jin, S., Jia, Y., 2020. Pan-tropical soil moisture mapping based on a three-layer model from CYGNSS GNSS-R data. *Remote Sens. Environ.* 247, 111944.
- Zeiger, P., Frappart, F., Darrozes, J., Prigent, C., Jiménez, C., 2022. Analysis of CYGNSS coherent reflectivity over land for the characterization of pan-tropical inundation dynamics. *Remote Sens. Environ.* 282, 113278 <https://doi.org/10.1016/j.rse.2022.113278>.
- Zhang, S., Ma, Z., Li, Z., Zhang, P., Liu, Q., Nan, Y., Zhang, J., Hu, S., Feng, Y., Zhao, H., 2021. Using CYGNSS data to map flood inundation during the 2021 extreme precipitation in Henan Province, China. *Remote Sens. (Basel)* 13, 5181.